HHS Public Access

Author manuscript

Cell Metab. Author manuscript; available in PMC 2022 March 02.

Published in final edited form as:

Cell Metab. 2021 March 02; 33(3): 629–648.e10. doi:10.1016/j.cmet.2020.12.003.

The Pyruvate-Lactate Axis Modulates Cardiac Hypertrophy and Heart Failure

Ahmad A. Cluntun[1,10], **Rachit Badolia**[2,10], **Sandra Lettlova**[1,10], **K. Mark Parnell**[3], **Thirupura S. Shankar**[2], **Nikolaos A. Diakos**[2,11], **Kristofor A. Olson**[1,12], **Iosif Taleb**[2], **Sean M. Tatum**[4], **Jordan A. Berg**[1], **Corey N. Cunningham**[1], **Tyler Van Ry**[1,5], **Alex J. Bott**[1], **Aspasia Thodou Krokidi**[2], **Sarah Fogarty**[1,9], **Sophia Skedros**[2], **Wojciech I. Swiatek**[1], **Xuejing Yu**[6], **Bai Luo**[7], **Shannon Merx**[3], **Sutip Navankasattusas**[2], **James E. Cox**[1,5], **Gregory S. Ducker**[1], **William L. Holland**[4], **Stephen H. McKellar**[6,8], **Jared Rutter**[1,9,13,*], **Stavros G. Drakos**[2,8,*]

[1]Department of Biochemistry, University of Utah, Salt Lake City, UT 84132, USA

[2]Nora Eccles Harrison Cardiovascular Research and Training Institute, University of Utah, Salt Lake City, UT 84112, USA

[3]Vettore Biosciences, 1700 Owens Street Suite 515, San Francisco, CA 94158, USA

[4]Department of Nutrition and Integrative Physiology and the Diabetes and Metabolism Research Center, University of Utah, Salt Lake City, UT 84112, USA

[5]Metabolomics, Proteomics and Mass Spectrometry Core Facility, University of Utah, Salt Lake City, UT 84112, USA

[6]University of Utah, School of Medicine, Salt Lake City, Utah; Division of Cardiothoracic Surgery, Department of Surgery, Salt Lake City, UT 84132, USA

[7]Drug Discovery Core Facility, University of Utah, Salt Lake City, UT 84112, USA

[8]U.T.A.H. (Utah Transplant Affiliated Hospitals) Cardiac Transplant Program: University of Utah Healthcare and School of Medicine, Intermountain Medical Center, Salt Lake VA (Veterans Affairs) Health Care System, Salt Lake City, UT, USA.

[*]Correspondence: rutter@biochem.utah.edu (J.R.), stavros.drakos@hsc.utah.edu (S.G.D).

Author Contributions

Conceptualization, A.A.C., R.B., S.N., S.H.M., J.R., and S.G.D.; Methodology, Validation, Formal Analysis, and Investigation, A.A.C., R.B., S.L., K.M.P., T.S.S., N.A.D., K.A.O., I.T., S.M.T., J.A.B., C.N.C., T.V.R., A.J.B., A.T.K., S.F., S.S, W.I.S, X.Y., B.L., S.M., S.N., and J.E.C.; Software, J.A.B.; Resources, K.M.P., W.I.S., X.Y., J.E.C., G.S.D., W.L.H., S.H.M., and S.G.D.; Data Curation, A.A.C., R.B., S.L., I.T. and J.A.B.; Writing - Original Draft, A.A.C., R.B., S.G.D, and J.R.; Writing - Review & Editing, A.A.C., R.B., S.L., S.F., S.N., S.H.M., J.R., and S.G.D.; Visualization, A.A.C., R.B., K.M.P, and J.A.B.; Supervision, J.R., and S.G.D.; Funding Acquisition, S.H.M., J.R., and S.G.D.

Declaration of Interests

The University of Utah has filed a patent related to the mitochondrial pyruvate carrier, of which J.R. is listed as co-inventor. JR is a founder of Vettore Biosciences and a member of its scientific advisory board. KMP is an employee and shareholder of Vettore Biosciences. SM was an employee of Vettore Biosciences. SGD is a consultant to Abbott (Steering Committee member of the INTELLECT-2 multicenter trial of LVAD and CardioMEMS). JR and SGD are the recipients of a grant from Merck related to mechanisms of HF and myocardial recovery. All other authors declare no competing interests.

[9]Howard Hughes Medical Institute, University of Utah School of Medicine, Salt Lake City, UT 84132, USA

[10]These authors contributed equally

[11]Present address: Division of Cardiology, Tufts Medical Center, Boston, MA 02111, USA

[12]Present address: Department of Surgery and Perioperative Care, Dell Medical School, University of Texas, Austin, TX 78712, USA

[13]Lead Contact

Summary

The metabolic rewiring of cardiomyocytes is a widely accepted hallmark of heart failure (HF). These metabolic changes include a decrease in mitochondrial pyruvate oxidation and an increased export of lactate. We identify the Mitochondrial Pyruvate Carrier (MPC) and the cellular lactate exporter Monocarboxylate Transporter 4 (MCT4), as pivotal nodes in this metabolic axis. We observed that cardiac assist device-induced myocardial recovery in chronic HF patients was coincident with increased myocardial expression of the MPC. Moreover, the genetic ablation of the MPC in cultured cardiomyocytes and in adult murine hearts was sufficient to induce hypertrophy and HF. Conversely, MPC overexpression attenuated drug-induced hypertrophy in a cell-autonomous manner. We also introduced a novel, highly potent MCT4 inhibitor that mitigated hypertrophy in cultured cardiomyocytes and in mice. Together, we find that alteration of the pyruvate-lactate axis is a fundamental and early feature of cardiac hypertrophy and failure.

Graphical Abstract

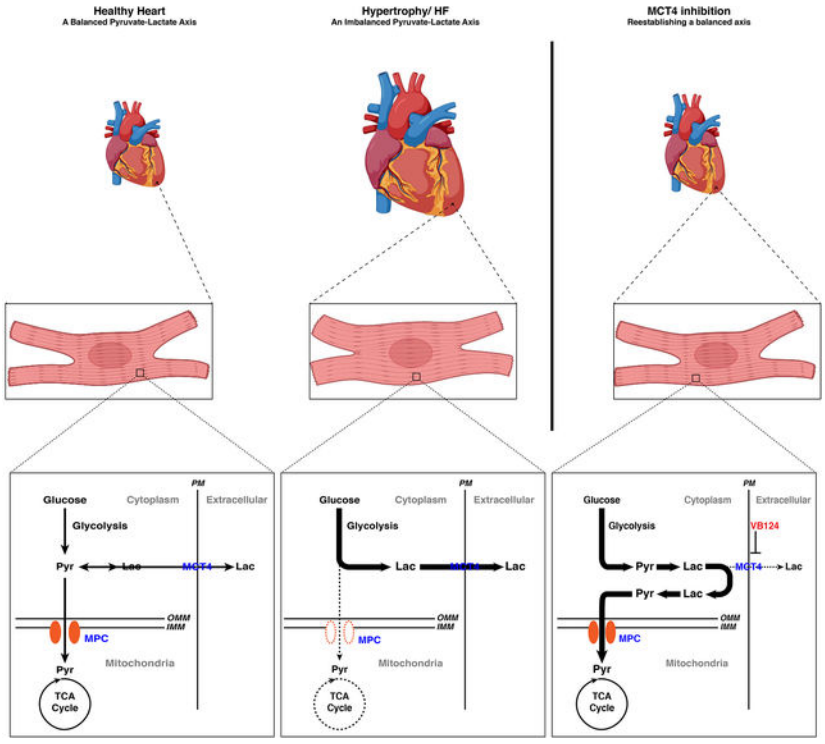

In Brief

Cluntun, et al identify the pyruvate-lactate axis as a critical node in cardiac homeostasis and health. This axis is maintained by a careful regulation of the disposition of pyruvate, including mitochondrial import and cellular export as lactate. During hypertrophy and HF, this balance is disrupted. Regaining this balance by inhibiting MCT4 ameliorated the hypertrophic phenotype.

Keywords

Heart Failure; Hypertrophy; LVAD; Responders; Non-Responders; Pyruvate; Lactate; Pyruvate-Lactate Axis; Cardiac Metabolism; Mitochondria; MPC; Phenylephrine; Isoproterenol; MCT4; VB124

Introduction

Heart failure (HF) is a complex and chronic heart disease characterized by a reduced capacity of the heart to pump or fill with blood, and is a leading cause of hospitalization and mortality worldwide (Savarese and Lund, 2017). The development of HF is typically preceded by pathological cardiac hypertrophy, a maladaptation that manifests as an increase in cardiomyocyte and heart size (Tham et al., 2015). Chronic HF has numerous etiologies (Jessup and Brozena, 2003, Metra and Teerlink, 2017), and frequently results from idiopathic cardiomyopathy (i.e. of unknown cause) (Kasper et al., 1994, McNally and Mestroni, 2017). Therapeutic options for patients with advanced HF are limited, but include invasive procedures such as heart transplantation and left ventricular assist device (LVAD) implantation, which restores adequate blood flow and hemodynamics via mechanical support (i.e. unloading) (Bekfani et al., 2018). Originally, LVADs were seen as either a temporary intervention while patients awaited a donor heart, or as a lifetime therapy (i.e. destination therapy). However, an increasing number of single center and multi-center reports have identified a subset of advanced, chronic HF patients (on average 15%, but ranging from 5–60% depending on the HF etiology and patient population) that undergo a significant degree of myocardial recovery following LVAD unloading and circulatory support (Drakos et al., 2017, Wever-Pinzon et al., 2016a, Wever-Pinzon et al., 2016b, Birks et al., 2011, Boehmer et al., 2012, Topkara et al., 2016, Birks et al., 2006, Dandel et al., 2008, Drakos et al., 2013). As a result, LVAD therapy has been proposed as a possible treatment for HF reversal (i.e. bridge-to-myocardial recovery) rather than bridge-to-transplant or destination therapy (Drakos et al., 2017). Nevertheless, the intrinsic reasons dictating why some chronic HF patients respond and others do not remain poorly understood.

Under normal conditions, cardiomyocyte metabolism is flexible and dynamic, with fatty acid oxidation (FAO) serving as the primary energy source for ATP production. In contrast, during HF cardiomyocytes lose their metabolic flexibility and shift away from FAO towards glycolytic metabolism that is uncoupled from pyruvate oxidation (Bertero and Maack, 2018, Kolwicz et al., 2013, Karwi et al., 2018, Tran and Wang, 2019). Instead of pyruvate being imported into the mitochondria, it is metabolized in the cytosol, primarily to lactate, but also to other metabolites such as amino acids. Despite this reproducible observation in human HF

and in animal models of the disease, the underlying causes of these metabolic changes and how they correlate with, predict or cause cardiac failure and recovery remains unclear.

Although often dismissed as a waste product, lactate is a normal myocardial fuel that can be converted into pyruvate via the enzyme lactate dehydrogenase (LDH), and thereby feed the tricarboxylic acid (TCA) cycle to produce ATP (Opie, 1980, Hui et al., 2017). Indeed, it was recently reported that glucose feeds the TCA cycle via circulating lactate, implicating lactate as an important energy source for the myocardium (Hui et al., 2017). This consumption of lactate is balanced by the concurrent production of lactate from glycolytic pyruvate in healthy human hearts (Bergman et al., 2009, Bing et al., 1953, Gertz et al., 1988, Wisneski et al., 1985). During HF, however, this balance is lost, as glycolytic pyruvate is preferentially converted to lactate, with a simultaneous decrease in lactate consumption (Fillmore et al., 2018, Diakos et al., 2016). We refer to this balance as the pyruvate-lactate axis.

The mitochondrial pyruvate carrier (MPC) is a heterodimeric complex of MPC1 and MPC2 that transports pyruvate (Bricker et al., 2012), the product of glycolysis, into the mitochondria where it can be fully oxidized via pyruvate dehydrogenase (PDH) and the TCA cycle. The MPC subunits are expressed at a high level in the normal adult heart (Uhlen et al., 2015). In contrast, under normal conditions, cardiomyocytes express low levels of MCT4, which is a member of the monocarboxylate transporter (MCT) family, which is believed to be the principal lactate exporter in cells (Price et al., 1998, McClelland and Brooks, 2002, Wilson et al., 1998, Zhu et al., 2013). As such, the MPC is likely a key control point at which the decision between pyruvate oxidation or cytosolic conversion to lactate is made. Here, we identify this pyruvate-lactate axis, as an important node for cardiac homeostasis and health.

We found that in chronic HF patients implanted with LVADs, cardiac recovery correlated with increased MPC abundance in heart tissue. Conversely, genetic depletion of the MPC in adult mice was sufficient to induce cardiac hypertrophy, chronic HF and death. Furthermore, loss of MPC activity was sufficient to induce hypertrophy while MPC overexpression mitigated drug-induced hypertrophy in multiple *in vitro* cardiomyocyte models. We also showed that the activity of the lactate exporter MCT4, which metabolically opposes the MPC, is required for hypertrophy. We introduced a novel and potent MCT4 inhibitor that prevented and reversed hypertrophy both in cultured cardiomyocytes and in mice. Using a combination of 13C-glucose flux experiments and compartment-specific metabolomics, we showed that decreased mitochondrial pyruvate oxidation is tightly linked to cardiomyocyte hypertrophy. Together, these data demonstrate that the pyruvate-lactate metabolic axis is a critical component in controlling cardiomyocyte growth and function and may direct insight into viable therapeutic concepts.

Results

MPC1 deficiency promotes cardiac hypertrophy and leads to heart failure

Following LVAD implantation and after several months of mechanical unloading and circulatory support, advanced, chronic HF patients were categorized as either responders or non-responders (Figure 1A). This designation was based on left ventricular ejection fraction

(LVEF) and left ventricular end-diastolic diameter (LVEDD) analyzed from serial echocardiography during diminished LVAD support (i.e. “LVAD turn-down” echocardiograms). Unlike non-responders, the responder group showed a significant post-LVAD increase in LVEF, a positive indicator of myocardial systolic function, and a significant decrease in LVEDD, an indicator of heart size (Figures 1B, 1C).

Responder status was defined as either final LVEF greater than 40% accompanied by reduction of LVEDD to less than 6.0 cm or relative improvement of LVEF >50 % and LVEDD < 6.0 cm. Non-responder status was defined as final LVEF <35% with <50% relative improvement in LVEF, regardless of LVEDD change. To define the mechanistic underpinnings of HF recovery in responders, we collected and analyzed left ventricular (LV) tissue from both sets of patients at the time of LVAD implantation and again at LVAD explant at the time of heart transplant (Figure 1A).

Compared to non-failing donor hearts, MPC1 was lower in the HF myocardial tissue samples obtained at the pre-LVAD (Pre) time point, for both responder and non-responder groups, although MPC1 abundance was more severely decreased in the responder group (Figure 1D). Interestingly, the abundance of MPC1 post-LVAD (Post) was differentially affected in the responder and non-responder groups. Specifically, when analyzing samples of cardiac tissue following LVAD support, we observed a post-LVAD increase in MPC1 abundance in the responder group, but no significant effect on MPC1 abundance in non-responders (Figures 1D and S1A–C). This was also confirmed by qRT-PCR (Figure S1D and S1E). The effect on MPC1 abundance was consistent with the inverse pattern that we observed in LVAD-responder hearts, but not those from non-responders, for the inhibitory phosphorylation of pyruvate dehydrogenase (p-PDH), which was dramatically elevated pre-LVAD and then reduced to near control levels post-LVAD (Figures 1E, S1F). Pyruvate oxidation appeared to be inhibited in non-responders both pre- and post-LVAD, as PDH was more highly phosphorylated compared to the donor control (Figure 1E). Table 1 shows baseline characteristics and echocardiographic changes observed in those patients whose myocardial samples were used for the molecular assays in Figures 1D, 1E and S1A–F (Table 1).

These data from human myocardial samples suggest that the subset of HF patients that respond to LVAD may have an underlying metabolic etiology contributing to their HF that is centered on defective mitochondrial pyruvate metabolism. Given that the MPC is low in HF patients and specifically increases in responders, we wanted to test whether altered MPC expression is causal for HF and recovery. To determine if loss of the MPC was sufficient to induce HF *in vivo*, we first generated a cardiac-specific and inducible *MPC1*-deficient mouse model (*MPC1*^{CKO}), using a floxed *MPC1* allele (Schell et al., 2017, Gray et al., 2015) and the α-MHC MerCreMer allele, which expresses tamoxifen-sensitive Cre-ER under the control of the cardiomyocyte-specific α-MHC promoter (Sohal et al., 2001). As expected, *MPC1*^{CKO} mice exhibited cardiac-specific and tamoxifen-inducible loss of MPC1 and MPC2 proteins (Figure 1F), consistent with previous reports from us and others that loss of one MPC subunit results in degradation of the other (Flores et al., 2017, Gray et al., 2015, Schell et al., 2017, Grenell et al., 2019, Rauckhorst et al., 2017).

Next, we performed serial echocardiography on these mice starting one week after tamoxifen treatment. M-mode echocardiography revealed that the *MPC1*^{CKO} mice were indistinguishable from WT littermates one week following tamoxifen injection. At 9 weeks post-induction (wpi), however, *MPC1*^{CKO} hearts exhibited dilated cardiomyopathy that progressed to overt heart failure by 16 wpi (Figure 1G). *MPC1*^{CKO} animals exhibited severely decreased LV function as indicated by a significant reduction in LVEF and fractional shortening (FS) at 9 wpi (Figures 1H and 1I). Additionally, *MPC1*^{CKO} animals demonstrated significantly increased heart size, as measured by LVEDD, compared to WT mice starting from 9 wpi (Figure 1J). Upon histological analysis, cross-sectional heart area was larger in the *MPC1*^{CKO} mice compared to WT (Figure 1K). The development of myocardial hypertrophy in the *MPC1*^{CKO} mice was also evidenced by the increase in the LV mass beginning at 13 wpi, with and without normalization to body weight (Figure 1L and S1G). We also observed an increase in expression of two hypertrophic markers, atrial natriuretic peptide (ANP) and B-type natriuretic peptide (BNP) in the *MPC1*^{CKO} mice (Figures S1H, and S1I). *MPC1*^{CKO} mice exhibited significant weight loss starting after 13 wpi (Figure 1M). Soon thereafter they began to perish and were all dead by 18 wpi (Figure 1N). These results demonstrate that loss of MPC1 in the hearts of adult mice leads to the development of cardiac hypertrophy and lethal HF.

Loss of MPC causes early hypertrophy and eventual mitochondrial failure

To investigate the progressive changes that occur after loss of myocardial MPC, we performed RNA-Seq on hearts from control and *MPC1*^{CKO} mice at 8 wpi (before hypertrophy) and 16 wpi (after HF). When we performed GO term analysis on the differentially up-regulated genes, comparing *MPC1*^{CKO} to WT, we observed a sustained up-regulation of gene classes involved in cardiac cell development, collagen organization, cell division, and wounding response, suggesting the initiation of pre-hypertrophy gene regulatory programs (Figures 2A and 2B). This was apparent at the 8-week time point and was further strengthened at the 16-week time point. When examining individual genes, increased expression of genes associated with cardiac hypertrophy and glycolysis was evident in the *MPC1*^{CKO} compared to the WT mice (Figures 2C–2F). Likewise, we observed a corresponding decrease in the expression of genes associated with TCA cycle enzymes in the *MPC1*^{CKO} mice (Figures 2G and 2H). We also observed dysregulation of a broader set of genes involved in pyruvate metabolism at both 8 and 16 wpi (Figures 2I and 2J).

Transmission electron microscopic (TEM) analysis of LV tissue from the *MPC1*^{CKO} mice showed relatively normal mitochondrial structure and volume density at 8 wpi (Figures 2K and S2A). However, analysis of LV tissue at 16 wpi revealed myocardial mitochondria with irregular cristae and higher staining intensity in *MPC1*^{CKO} mice (Figure 2L). These structural defects were associated with a significantly lower mitochondrial volume density in *MPC1*^{CKO} at 16 wpi (Figure S2B). Together, these data suggest that loss of the MPC elicits early compensatory changes in the expression of metabolic genes, but eventually these fail and lead to overt mitochondrial defects that are coincident with HF and death (Figure 2M).

Loss of mitochondrial pyruvate transport is necessary and sufficient to induce hypertrophy in cardiomyocytes

To elucidate the early changes caused by MPC loss that might underlie the pathological hypertrophy observed in *MPC1*^{CKO} mice, we first employed H9c2 cultured cells, a simple model that can be differentiated into a cell with many features of a cardiomyocyte (Watkins et al., 2011, Zordoky and El-Kadi, 2007, Branco et al., 2015). We utilized the MPC-specific inhibitor UK5099 (UK), or doxycycline-inducible MPC1 shRNA-mediated knockdown (MPC1 KD) to impair MPC activity in these cells (Figure S3A). We found that either treatment caused an increase in cell size and total protein content (Figures 3A, 3B, and S3B–S3D). This effect was rapid, as UK treatment for as little as 24 hours was sufficient to induce a marked increase in cell size (Figures 3A and S3C). Furthermore, the expression levels of the hypertrophy markers ANP and BNP were both increased in the UK-treated cells (Figure S3E).

Next, we stably transduced H9c2 cells either with a vector overexpressing MPC1 and MPC2 (MPC OE) or with a control empty vector (EV) (Figure S3F). If loss of MPC activity is indeed an early insult predisposing for cardiomyocyte hypertrophy, overexpression of the MPC might confer resistance to hypertrophy-inducing drugs. Accordingly, we treated our MPC OE and EV cells with the known hypertrophy-inducing drugs Phenylephrine (PE), Isoproterenol (ISO), and Angiotensin (ATII), as well as the MPC inhibitor UK. We found that MPC OE prevented or mitigated cellular hypertrophy induced by all four of these agents (Figures 3C and S3G). Given that PE, ISO, and ATII all induce hypertrophy via distinct signaling mechanisms (Dzimiri, 1999, Ito et al., 1993, Clerk and Sugden, 1999), we hypothesize that decreased MPC function and the concomitant perturbation of the pyruvate-lactate axis are common downstream mediators of drug-induced cardiomyocyte hypertrophy.

It is important to note that the MPC is a protein complex that transports cytoplasmic pyruvate into the mitochondrial matrix, and has no intrinsic enzymatic activity. Thus, it would seem that severing this connection is sufficient to promote hypertrophy. To confirm this, we analyzed changes in carbohydrate metabolic fluxes in the same aforementioned experimental conditions using ^{13}C-glucose tracing (Figure 3D). In the UK-treated, MPC1 KD, and PE-treated H9c2 cells, we observed an increase in intra- and extracellular ^{13}C-labeled lactate, combined with an overall decrease in ^{13}C-labeled citrate of the TCA cycle (Figures 3E–G and S3H). These metabolic perturbations were expected upon inhibition or knockdown of MPC expression, but were also observed upon treatment with PE (Figure S3I). The necessity of this metabolic shift for hypertrophy was further supported by the observation that MPC OE rescued the PE-induced loss of ^{13}C-enrichment of TCA cycle intermediates from labeled glucose, coincident with preventing cellular hypertrophy (Figure 3G).

Primary cultured adult mouse cardiomyocytes (ACM) are a well-validated cardiomyocyte model that more faithfully recapitulates aspects of cardiomyocyte biology than H9c2 cells. Similar to H9c2 cells, we observed a substantial increase in cell surface area in WT cells treated with PE, ISO, and UK compared with vehicle (Veh) treatment (Figures 3H and 3I). Furthermore, we also observed a similar diversion of glycolytic carbon flux towards lactate

production and away from citrate production in a ^{13}C-glucose tracing experiment (Figures 3J and 3K).

To better understand the relationship between changes in metabolic flux, hypertrophy, and HF, we isolated and cultured ACMs from inducible cardiac-specific *MPC1*^{CKO} mice. Confocal microscopy analysis revealed hypertrophy in *MPC1*^{CKO} cells, akin to H9c2 cells with inhibited MPC activity, but this specifically manifested as an increase in the width-to-length ratio (Figures S3J–S3L). We isolated cardiomyocytes both before myocardial structural or functional abnormalities were apparent (12 wpi) and after onset of HF (16 wpi) and conducted a ^{13}C-glucose metabolic tracing experiment (Figures 4A and 4B). Consistent with loss of MPC activity, we observed an increase in extracellular lactate and a modestly decreased labeling of citrate in 12 wpi *MPC1*^{CKO} ACMs (Figure 4C). At this early timepoint (12 wpi), the labeling of the TCA cycle intermediates fumarate and succinate was unaffected (Figure 4C). Intriguingly, we observed normal labeling of alanine (Figure 4C), whose cytosolic production and mitochondrial import can act as an alternative MPC-independent mechanism through which glycolytic carbon can feed the TCA cycle (Gray et al., 2015, McCommis et al., 2015, Sharma et al., 2019). In cardiomyocytes isolated at the later timepoint (16 wpi), however, glucose flux into the TCA cycle was completely abolished, alanine labeling was decreased, and lactate export was further accelerated (Figure 4D). Taken together, these data demonstrate that decreased mitochondrial pyruvate uptake is sufficient to cause cardiomyocyte hypertrophy *in vitro*. Moreover, we found that hypertrophic signaling became completely inconsequential to cell size when the rebalancing of the pyruvate-lactate metabolic axis was prevented.

Identification of a potent and selective MCT4 inhibitor

Recent reports have indicated that MCT4 levels may increase during hypertrophy and HF to help jettison lactate from the cell (Zhu et al., 2013). Indeed, we found that hypertrophic PE-, ISO-, ATII-and UK-treated H9c2 cells exhibited increased MCT4 protein abundance (Figure S4A), which is consistent with these cells exhibiting decreased mitochondrial pyruvate flux and instead using MCT4-mediated lactate export to dispose of glycolytic carbon.

Therefore, we developed VB124 as a potent and selective MCT4 inhibitor that could specifically inhibit lactate efflux and might therefore redirect glycolytic carbon flux into mitochondrial pyruvate oxidation (Figure 5A). We performed a CRISPR/Cas9-based synthetic lethality screen to interrogate the genetic sensitivities conferred by VB124 treatment (Figures S4B and S4C). Strikingly, nearly all of the genes found to be synthetically lethal with VB124 functioned in mitochondrial oxidative phosphorylation. Conversely, nearly all genes whose deletion was “buffering” or “rescuing” upon VB124 treatment functioned in glucose transport and the early steps in glycolysis that precede reduction of NAD^+ to NADH (Figure S4D). These results are in strong agreement with previous reports of a synthetic lethal relationship between MCT-mediated lactate export and mitochondrial oxidative phosphorylation (Marchiq et al., 2015, Benjamin et al., 2018), due to effects on NAD^+ depletion (Benjamin et al., 2018, Marchiq et al., 2015). As predicted by the results of the synthetic lethality screen, we observed a strong synergistic effect on MDA-MB-231 cell proliferation when MCT4 inhibition was combined with any one of three

distinct OXPHOS inhibitors (Figure S4E). VB124 blocked lactate import (IC_{50} = 8.6 nM) and export (IC_{50} = 19 nM) in MDA-MB-231 cells that were engineered to express MCT4 as the only major plasma membrane lactate transporter (Figures S4F and S4G). VB124 is highly selective for MCT4 over MCT1, showing very little MCT1 inhibitory activity (IC_{50} = 24 μM) in MCT1-expressing BT20 cells (Figure S4H). Treating mice with a super-efficacious dose of VB124 (30 mg/kg BID/twice per day) for 180 days had no effect on body, heart, liver, or lung weight (Figures S4I–S4L), suggesting no overt toxicities. Together these data identify VB124 as a safe, selective, and potent MCT4 inhibitor.

MCT4 inhibition can prevent and reverse cardiomyocyte hypertrophy

MCT4 inhibition has been suggested as a potential target to counteract the aerobic glycolysis metabolic program and thereby impair tumor growth in different cancer types (Todenhofer et al., 2018, Benjamin et al., 2018, Lim et al., 2014, Dell'Anno et al., 2020). Given the similarities between the metabolic rewiring observed in both cancer and HF, we hypothesized that blocking lactate efflux in hypertrophied cardiomyocytes, via MCT4 inhibition, would lead to redirecting of glycolytic carbon flux back towards mitochondrial pyruvate oxidation and might reverse the hypertrophic phenotype (Figure 5A). To test this hypothesis, we first treated H9c2 cells simultaneously with both PE and the MCT4 inhibitor VB124 for 48 hours and found that MCT4 inhibition completely prevented PE-induced cellular hypertrophy (Figure 5B). To determine if MCT4 inhibition could not merely prevent PE-induced hypertrophy but also reverse it, we pretreated H9c2 cells with PE for 48 hours followed by a combination of PE and VB124 for an additional 48 hours (Figure 5B). MCT4 inhibition completely reversed the hypertrophic phenotype in these cells (Figure 5B). We next treated ACMs with PE and ISO and found that VB124 also mitigated the hypertrophic phenotype in these cells (Figures 5C and 5D). These effects of MCT4 inhibition, along with the anti-hypertrophic effects of MPC overexpression, highlight the importance of mitochondrial pyruvate metabolism in cardiomyocytes and are reminiscent of the increased MPC abundance that we observed in the responder LVAD treated patients.

^{13}C-glucose tracing experiments revealed that VB124 prevented the metabolic aberrations induced by treatment with PE or ISO in both H9c2 and ACM cells. In particular, VB124 decreased glucose flux towards lactate and increased glucose flux into citrate and the TCA cycle (Figures 5E–5G). This increased TCA cycle flux was also found in the cells that had been pretreated with PE and subsequently reversed with VB124 treatment (Figure S5A). Treatment with VB124 prevented the increased flux from glucose into pyruvate and intra- and extracellular lactate observed in PE- and ISO-treated cardiomyocytes (Figures 5G, S5B and S5C). Taken together, these data suggest that restored mitochondrial pyruvate metabolism reverses drug-induced cardiomyocyte hypertrophy.

Maintaining mitochondrial pyruvate prevents hypertrophy in cardiomyocytes

One of the major limitations of conventional metabolomics experiments is the fact that they cannot distinguish between different intracellular pools of a given metabolite. In particular, we wanted to test whether hypertrophic drugs as well as manipulations of MPC and MCT4 activity had compartment-specific effects on metabolite abundances and fluxes. To this end, we generated H9c2 cells stably expressing a mitochondria-specific 3XHA-GFP-Omp25 tag

(Mito-tag) that enables rapid isolation and extraction of mitochondria, which is necessary to reliably quantify metabolite pools within this organelle (Chen et al., 2016, Chen et al., 2017). In these enriched mitochondrial fractions (Figure S6A), we detected a decrease in steady-state pyruvate levels upon hypertrophic stimuli that was restored upon MCT4 inhibition (Figure 6A). However, we were unable to detect any lactate in the mitochondrial fraction, consistent with the notion that lactate is principally a cytosolic metabolite (Figure 6A). This pattern of mitochondrial pyruvate abundance was the inverse to that found in the whole cell extract, where UK and hypertrophic stimuli caused an increase in pyruvate and lactate that was reversed by MCT4 inhibition (Figure 6B). To confirm that this pyruvate was of glycolytic origin, we paired the Mito-tag approach with ^{13}C-glucose tracing and observed an enrichment of the M+3 pyruvate isotopomer in the untreated cells, which was undetectable upon UK, PE, and ISO treatment, but re-emerged upon MCT4 inhibition (Figure 6C). Consistent with the previous experiments, we could not detect any labeled lactate within the mitochondria in any condition, suggesting that glycolysis-derived pyruvate and not lactate enters the mitochondria and fuels the TCA cycle in these cells (Figure 6C). This finding is congruent with recent reports showing that either pyruvate or lactate alone is sufficient to keep cardiomyocytes viable in glucose-free media, assuming that lactate can be converted to pyruvate in the cytosol (Ritterhoff et al., 2019, Shao et al., 2018). We also performed a time-resolved ^{13}C-glucose tracing experiment on these Mito-tag cells and again observed increased flux into the TCA cycle from glycolysis upon VB124 treatment (Figures 6D–6F).

In addition to changes in the pyruvate-lactate axis, we also observed an increase in steady-state mitochondrial glutamate abundance and a decrease in mitochondrial aspartate in PE-, ISO-, and UK-treated cells (Figure 6G). Upon MCT4 inhibition, mitochondrial aspartate and glutamate abundances were completely normalized (Figure 6G). This pattern is exactly opposite to that observed in whole cell lysates (Figure 6H), further emphasizing the importance of deciphering compartmentalized mitochondrial metabolism in cardiomyocytes.

Increased glycolytic flux and decreased cellular respiration are common observations in hypertrophic cardiomyocytes (Zhou and Tian, 2018, Abel and Doenst, 2011). Mitochondrial membrane potential is required for ATP production, protein import, and is generally a reliable marker of overall mitochondrial health (Harbauer et al., 2014, Chacinska et al., 2009, Zorova et al., 2018). In agreement with this, we observed decreased mitochondrial membrane potential, as measured by the ratio of MitoTracker Red to MitoTracker Green fluorescence, upon ISO treatment in primary adult cardiomyocytes, which was completely rescued by VB124 treatment (Figures 6I, S6B–S6D). Moreover, we also observed elevated reactive oxygen species in these cells upon hypertrophic stimuli, which were also normalized with MCT4 inhibition (Figures 6J, S6E). Taken together these results reveal that MCT4 inhibition can reverse and attenuate cellular hypertrophy in cardiomyocytes and normalize mitochondrial oxidative metabolism.

MCT4 inhibition attenuates isoproterenol-induced cardiac hypertrophy in mice

Given that MCT4 inhibition prevented cardiomyocyte hypertrophy upon treatment with PE, ISO, and UK *in vitro*, we sought to determine whether the same might be true in animal

models of cardiac hypertrophy. Therefore, we surgically implanted mice with osmotic minipumps that continuously deliver either Veh or ISO to induce hypertrophy and simultaneously treated these mice with VB124 or Veh via daily oral gavage for 4 weeks (Figure 7A). We performed echocardiography on these mice at the end of the 4 weeks and collected their hearts after sacrifice. As expected, ISO infusion caused a significant increase in the heart-to-body weight ratio, which was prevented when MCT4 was additionally inhibited (Figures 7B and S7A). Furthermore, the increase in LVEDD upon ISO treatment was also absent in the MCT4 inhibitor-treated mice (Figure 7C). We also evaluated the LV volumes (end diastolic volume, EDV, and end systolic volume, ESV) which serve as a measure for heart size, and observed a similar increase with ISO treatment that was normalized upon MCT4 inhibition (Figure S7B and S7C). VB124 treatment had no significant effect on body weight for the duration of this experiment, consistent with the previous demonstration of safety at higher doses (Figure S7D). Despite significant changes in cardiac size, neither ISO nor VB124 had any significant effect on heart function as assessed by LVEF and fractional shortening during the limited time course of this study (Figure S7E and S7F).

Unbiased hierarchical clustering of the metabolic signatures of whole hearts isolated from these ISO and VB124-treated mice revealed unique metabolic changes due to ISO treatment that were prevented with VB124 treatment (Figure 7D). Indeed, inhibiting MCT4 activity was sufficient to revert the metabolic profile of ISO treated mice hearts back to resemble the profile of untreated controls as visualized by principal component analysis (Figure 7E). Specifically, we observed increased glycolytic intermediates upon ISO-induced hypertrophy that returned to control levels in mice treated with VB124 (Figure 7F). The abundances of proteins related to the pyruvate-lactate axis was consistent with these metabolic phenotypes. We observed increased expression of LDHA in the hearts of mice treated with ISO, consistent with increased lactate production (Figure S7G and S7H). Interestingly, similar to the responder LVAD patients, we also noted that ISO caused a significant decrease in MPC1 levels, which was restored upon VB124 treatment (Figures S7H and S7I).

Finally, TEM analysis on myocardium revealed that ISO treatment caused mitochondrial structural aberrations, which were ameliorated by VB124 treatment (Figure 7G). This included a decrease in mitochondrial area and volume density upon ISO treatment, which were both restored by MCT4 inhibition (Figures 7H and 7I). The number of inter-mitochondrial junctions (IMJs) is an index of highly active cardiac mitochondria (Picard et al., 2015), and we observed a significant decrease in IMJs in ISO-treated mitochondria, which was restored upon VB124 treatment (Figure 7J). Together, these data demonstrate that MCT4 inhibition reverses many of the pathological features of ISO-induced cardiac hypertrophy, including metabolic perturbations and mitochondrial structural impairment.

Discussion

Although changes in cardiac metabolism during hypertrophy and chronic HF are well documented (Barger and Kelly, 1999, Allard et al., 1994, Ritterhoff and Tian, 2017), these changes are often viewed as a compensatory or merely coincidental phenomenon rather than a cause of the disease, and thus have rarely been considered as a viable target for treatment.

We set out to test the hypothesis that, instead, these metabolic changes play a causal role in driving pathological cardiac hypertrophy and eventual heart failure. Consistent with this hypothesis, we found a tight coupling between the abundance of the MPC and myocardial recovery in a clinical chronic HF population treated with LVAD unloading. For the purposes of this study we proceeded with heart transplantation even in responders, which is the standard of care therapy for advanced HF patients. Future studies will examine the alternative option to remove the LVAD and abort the plan for heart transplantation as a therapeutic option. Recent studies have independently demonstrated decreased abundance of the MPC subunits in HF patients (Sheeran et al., 2019). However, the subsequent increase in MPC abundance upon myocardial recovery from chronic HF is a novel finding that demonstrates an intimate relationship between the pyruvate-lactate axis and cardiac function in humans, both during the progression towards chronic HF and in LVAD-induced myocardial recovery.

This notion that the subset of HF patients that improve their myocardial function and structure upon LVAD unloading might have a particular form of HF that is intimately associated with metabolic aberrations is supported by our recent observation that cardiac recovery correlated to specific metabolic changes that not only increase energy production but also increase channeling into cardio-protective pathways (Badolia et al., 2020).

How could metabolic changes play a causal role in HF?

We observed that loss of MPC activity and the resulting imbalance of the pyruvate-lactate axis was sufficient to cause cellular hypertrophy. These were cell-autonomous effects in both H9c2 cells and primary cardiomyocytes using validated genetic and pharmacological approaches that target the MPC. In all cases, this was accompanied by decreased labeling of TCA cycle intermediates from ^{13}C-glucose and increased production and export of lactate. Intriguingly, this metabolic pattern was indistinguishable from that caused by treatment with pharmacological agents (including PE and ISO) that induced hypertrophy via various signaling mechanisms.

Furthermore, chronic four-week treatment with ISO, in mice, caused an increase in heart size as assessed both by the heart-to-body weight ratio as well as by LVEDD measurements. Without any obvious adverse effects, inhibition of the MCT4 lactate exporter completely prevented this cardiac hypertrophy. It is worth noting that, although MCT4 inhibition clearly elicited structural myocardial benefits, improvements to cardiac function were less evident, at least not for the duration of our experiment. However, many current approved first-line HF drug therapies have minimal or neutral effects on the systolic LV function and LVEF but still manage to significantly improve the outcomes of chronic HF patients (Yancy et al., 2017, Khattar et al., 2001).

MCT4 inhibition can prevent cardiac hypertrophy

In this manuscript, we introduce a safe, potent and effective inhibitor of the MCT4 lactate exporter. Although MCT4 exhibits low expression in most cell types, including cardiomyocytes (Bonen, 2001, Bisetto et al., 2019), it is frequently induced under pathological scenarios. In the heart, MCT4 expression has been shown to be induced during

myocardial injury (Zhu et al., 2013, Gabriel-Costa et al., 2018) and in hearts perfused with lactate (Gabriel-Costa et al., 2015). Furthermore, knocking out CD147, a broadly expressed plasma membrane glycoprotein known to be necessary for MCT4 function and localization (Kirk et al., 2000), has been recently reported to attenuate heart injury after pulmonary embolism and chronic pressure overload (Lu et al., 2018, Suzuki et al., 2016). Our observations of the efficacy of MCT4 inhibition to prevent cardiomyocyte hypertrophy raise the possibility of such a therapeutic strategy in humans.

The pyruvate-lactate metabolic axis

Integral to our approach was, first, that lactate dehydrogenase (LDH) is a bidirectional enzyme that is regulated by the concentrations of its substrates: lactate and pyruvate (Spriet et al., 2000). Moreover, LDHA activity is important for cardiac hypertrophic growth (Dai et al., 2020). Inhibiting lactate export leads to an intracellular build-up of lactate that pushes LDH in the reverse direction towards pyruvate accumulation, while producing NADH as a by-product of this reaction. In turn, accumulation of pyruvate drives its entry into the mitochondria via the MPC (or other alternative routes), where it can inhibit the enzyme pyruvate dehydrogenase kinase (PDK) (Sugden and Holness, 2003). This impedes the ability of PDK to suppress pyruvate dehydrogenase (PDH) activity, thus increasing the cells' ability to oxidize pyruvate.

An unexpected by-product of the build-up of pyruvate and lactate was a decrease in intracellular ROS. This could be due to the ability of lactate and pyruvate to scavenge free radical species (Liu et al., 2018, Groussard et al., 2000, Herz et al., 1997). Indeed, pyruvate and lactate have been previously reported to protect myocardium from oxidant stress (Yanagida et al., 1995, de Groot et al., 1995). Damaged mitochondria have been identified as a precursor to heart failure (Wai et al., 2015, Acin-Perez et al., 2018), and the improvement in mitochondrial membrane potential and overall mitochondrial health with MCT4 inhibition add to a growing body of evidence linking mitochondrial health to cardiac health (Brown et al., 2017, Zhou and Tian, 2018, Lesnefsky et al., 2001). Our data in multiple systems demonstrate the importance of mitochondrial pyruvate metabolism for maintenance of mitochondrial structure and function and to limit the production of reactive oxygen species in cardiomyocytes.

Compartmentalization of aspartate and glutamate are greatly affected by the pyruvate-lactate axis

Recent reports have suggested that glucose-derived aspartate is important to drive biomass synthesis and pathological cardiac hypertrophy (Ritterhoff et al., 2019). Our study introduces an additional level of complexity to this model by distinguishing the cytosolic and mitochondrial aspartate pools. Both aspartate and glutamate have been reported to increase during pressure overload models in mice despite a decrease in TCA cycle intermediates (Umbarawan et al., 2018). In contrast, we observed reciprocal changes in aspartate and glutamate levels between the mitochondrial and cytosolic compartments in response to hypertrophic stimuli. This phenomenon is consistent with the function of the mitochondrial aspartate-glutamate antiporter, which exchanges aspartate for glutamate across the mitochondrial inner membrane (Palmieri, 2013). Upon hypertrophic drug

treatment, cytosolic aspartate pools are increased, which has been shown to support hypertrophic growth (Figure S7J). For reasons we currently don't understand, inhibiting lactate export might cause a diversion of the metabolic flux away from cytosolic aspartate accumulation to feed the TCA cycle, which could then increase the mitochondrial aspartate pool via oxaloacetate. In this scenario, the decreased mitochondrial glutamate pools suggest that this antiporter may be functioning in reverse, however, further studies are required to confirm this observation (Figure S7K). Moreover, it has recently been shown that this antiporter activity can be increased by the presence of pyruvate, consistent with the observed impact of UK and VB124 (Birsoy et al., 2015, Sullivan et al., 2015, Chen et al., 2016). The idea that a mitochondria-specific pool of pyruvate might regulate the mitochondrial aspartate-glutamate antiporter in cardiomyocytes and modulate the localization of aspartate and glutamate provides potential mechanisms underlying the observed hypertrophic response. The increased mitochondrial import of aspartate may shuttle some of the cytoplasmic aspartate away from processes that would use it to support hypertrophic metabolism, like protein and nucleotide biosynthesis (Gui et al., 2016, Safer, 1975). The effects of this aspartate sequestration phenomenon may be amplified by the high density of mitochondria present in cardiomyocytes (Barth et al., 1992). The importance of cytosolic aspartate availability in supporting cardiomyocyte hypertrophy and the regulatory role of mitochondrial pyruvate warrant further *in vivo* investigation.

Previous work on mitochondrial pyruvate metabolism in the heart focused primarily on the PDH enzyme (Gopal et al., 2018, Seymour and Chatham, 1997). Our study highlights the importance of the MPC, which precedes the PDH by importing the PDH substrate pyruvate, and appears to have many of the same metabolic consequences. This transition to a low MPC state characterized by a glycolytic metabolic phenotype has been observed as a common feature of solid tumors, where it is believed to promote a biosynthetic program to sustain the biomass needs of cell proliferation. In particular, we recently identified the loss of the MPC as an early insult promoting hyperproliferation and eventual tumor formation in the colon (Bensard et al., 2020). Primary cardiac tumors are exceedingly rare (Cresti et al., 2016). Our results raise the possibility, however, that the same metabolic perturbation that drives cellular proliferation in tumor-initiating cells in the colon might also be driving cellular hypertrophy in post-mitotic cardiomyocytes.

Limitations of Study

In this study, all chronic HF patients, regardless of their subsequent recovery status, have end-stage HF caused by various etiologies. Myocardium samples acquired from these LVAD patients accrue over time and are also finite, which led to variation in the patient population between some of our experiments. Regarding the mouse studies, isoproterenol infusion, although appropriate for our study, is not a standard model for HF induction in the field. Therefore, future studies are warranted to address the efficacy of MCT4 inhibition to ameliorate HF in complementary models. We have also used genetic manipulations and treatment with chemical inhibitors to induce hypertrophy and HF in cultured cells and mice. While these manipulations reliably induce hypertrophy and HF in these models, they generate a scenario where all animals and cells exhibit hypertrophy and HF within a relatively short period of time. Future studies should address the degree to which a change in

the cardiomyocyte metabolic profile predisposes it for hypertrophy and HF in settings that are more akin to human chronic HF.

STAR METHODS

RESOURCE AVAILABILITY

Lead Contact—Further information and requests for resources and reagents should be directed and will be fulfilled by the Lead Contact, Jared Rutter (rutter@biochem.utah.edu).

Materials availability—Mouse and cell lines generated in this study are available for any researcher upon request.

Data and Code availability—Sequencing data have been deposited at NCBI Gene Expression Omnibus (http://www.ncbi.nlm.nih.gov/geo) under accession number GSE152055. Scripts used to perform these analyses can be found at https://github.com/j-berg/cluntun_analysis_2020.

EXPERIMENTAL MODEL AND SUBJECT DETAILS

Human subjects—Patients with chronic advanced HF were prospectively enrolled at the time of LVAD implantation. All the subjects enrolled (age ≥ 18-years, irrespective of gender) in the study are end-stage heart failure patients with NYHA functional class III or IV and clinical characteristics consistent with dilated cardiomyopathy and chronic advanced heart failure who required LVAD support as a bridge to transplantation. Patients with acute HF (acute myocardial infarction, acute myocarditis, post-cardiotomy cardiogenic shock, and so on) were prospectively excluded from the study. The average age of the study population is 51 years and includes both males and females, with majority of the patients being males (75%). Patients are either ischemic (43.5%) or non-ischemic (53.6%) with almost equal distribution and have an average duration of HF symptoms of 5 years. Patients who received LVAD due to confirmed acute HF etiologies and had no past medical history of chronic HF were prospectively excluded from the study population. Control tissue was acquired from Donors (ND) with non-failing hearts (based on echocardiography) that were not allocated for human heart transplantation due to non-cardiac reasons such as size mismatch, infectious diseases and other. This study was carried out at institutions comprising the U.T.A.H. (Utah Transplantation Affiliated Hospitals) Cardiac Transplant Program (University of Utah Health Science Center, Intermountain Medical Center, and the George E. Wahlen VA Medical Center, Salt Lake City, Utah). The institutional review board of each institution approved the study, and all patients provided informed consent.

Animals and animal care—Animal work was performed in accordance with the University of Iowa Animal Care and Use Committee (IACUC). Generation of adult cardiac-specific MPC1-knock out mice, A C57BL/6 MPC1 fl/fl mice was generated as previously described (Schell et al., 2017) and crossed with αMHC-Cre-ER(T2). MPC1 fl/+; αMHC-Cre-ER(T2) were crossed to MPC1 fl/+; αMHC-Cre-ER(T2) to produce MPC1 fl/fl; αMHC-Cre-ER(T2) and WT littermates. The 8-week-old MPC1 fl/fl; αMHC-Cre-ER(T2) and WT littermates were injected intraperitoneally with 40 mg/ kg of body weight tamoxifen

for 3 consecutive days to yield adult cardiac-specific MPC1 knock out and WT littermates. Wild type littermates were used as controls.

Adult Cardiomyocyte isolation—Adult mice were anesthetized with sodium pentobarbital (50mg/kg) and the excised heart was attached to an aortic cannula and perfused with solutions gassed with 100% O_2 and held at 37°C, pH 7.3. Perfusion with a 0 mM Ca^{2+} solution for 5 mins was followed by 15 min of perfusion with the same solution containing 1mg/ml collagenase and 0.1mg/ml protease. The heart was then perfused for 1 min with stopping solution (the same solution containing 20% serum and 0.2 mM $CaCl_2$). All perfusions were performed at a flowrate of 2ml/min. The atria were removed and the ventricles were minced and shaken for 10 min, and then filtered through a nylon mesh. Cells were stored at 37°C in normal HEPES buffered solution. All myocytes used in this study were rod-shaped, had well-defined striations, and did not spontaneously contract.

Adult Cardiomyocyte Culture—Isolated primary adult cardiomyocytes were enriched by gravity sedimentation in increasing concentrations of Ca^{2+} DMEM plating media containing: Primocin, Penicillin streptomycin, HEPES, 5% Fetal Bovine Serum, and 10mM 2,3-Butanedione monoxime. Cells were plated on Laminin coated petri dishes or coverslips, and allowed to adhere for at least 1hour in the incubator. Cells were then switched to DMEM Culture media containing: Primocin, Penicillin streptomycin, HEPES, Insulin-Transferrin-Selenium, 0.1 mg/ml of Bovine serum albumin, and chemically defined lipid concentrate. Cells were cultured in a final Ca^{2+} of 1mM.

Cell lines—H9c2 myoblastic cell line, BT20 and MDA-MB-231 were purchased from ATCC and routinely maintained in DMEM media supplemented with 10% FBS and 1% PenStrep in 5% CO_2 and 37°C. H9c2 myoblastic cells were differentiated into cardiomyocytes by cultivating in DMEM supplemented with 1% FBS, 1% PenStrep and 10 μM retinoic acid for 5 days. Then the cells were washed with 1x PBS and treated with drugs for indicated period in DMEM supplemented with 1% FBS and 1% PenStrep.

Mito-tag H9c2 cells—This protocol is as described in (Chen et al., 2017) with minor changes. Briefly, H9c2 rat cardiomyoblast cells were transduced with 3XHA- or-3XMyc-GFP-Omp25 retroviruses and selected by flow cytometry for lowest 20% positive GFP cells. 3XHA-GFP-Omp25 H9C2 cells were treated with appropriate concentrations of inhibitors for 1–2days as indicated within the text. Cells were grown to confluency in 150mm plates (6 plates/condition/experiment, each experiment was repeated 3 times), washed with LC/MS PBS, and harvested in LC/MS grade KPBS (136mM KCl, 10mM KH_2PO_4, pH 7.25) with 1 mM PMSF. Cells were Dounce-homogenized with 25 strokes of the plunger, centrifuged, and the supernatant containing mitochondria was immunoprecipitated for 3.5 minutes using HA-magnetic beads. IP was washed three times with KPBS and metabolites were extracted with 80% LC/MS Grade-methanol solution precooled to −80°C. All steps were performed in a 4°C cold room.

METHOD DETAILS

Knockdown and overexpression strategies—For overexpression of MPC1 and MPC2, the HA-MPC2-P2A-T2A-MPC1-FLAG sequence was cloned into retroviral vector pQXCIP. The retroviral particles were produced by co-transfection of 293T cells with Gag-Pol and VSVG packaging plasmids using polyethylenimine (PEI) as a transfection reagent (3:1 mass ratio of PEI:DNA). Virus-containing medium was collected after 48 h, filtered through 0.45 μm filter, aliquoted and stored in −80°C. To induce overexpression, retrovirus containing supernatant was added to cells grown in normal culture medium together with polybrene transfection reagent in concentration 8–10 μg/mL. The transduced cells were selected by puromycin and the level of overexpression was assessed by western blotting (WB). piSMART mCMV/TurboGFP vector containing doxycycline inducible shRNA against MPC1 or non-targeting were purchased from Dharmacon (GE Healthcare). Lentiviral particles carrying piSMART mCMV-GFP shMPC1 vector were produced in 293T cells using second generation psPAX and pMD.2G plasmids and polyethylenimine (PEI) as a transfection reagent. H9c2 cell line expressing shRNA against MPC1 after induction with doxycycline was generated by transduction of cells with above described lentiviral particles and puromycin selection.

Control-MITO or HA-MITO constructs containing either 3x MYC or 3x HA epitope tags joined to the N-terminus of EGFP, which is then fused to the outer mitochondrial membrane localization sequence of OMP25 were gifts from Dr. David M. Sabatini. H9c2 cells stably expressing Control-MITO or HA-MITO tags were prepared by transduction with retroviral particles carrying these vectors (preparation described above) and selection with blasticidin.

Tissue lysates—Proteins from human LV tissues or mouse ventricular tissues were extracted using RIPA lysis buffer containing HALT Protease and Phosphatase inhibitor cocktail solution (Pierce, Rockford, IL). After homogenization using a bead-homogenizer, tissue lysates were incubated on ice for an hour. Samples were centrifuged at 14,000g for 30 minutes at 4°C. The supernatant was collected and protein estimation was performed using Pierce BCA Protein Assay Kit (Thermo Scientific, Rockford, IL) before equal volume of 2x sample buffer containing 1 mM DTT was added.

Cell lysate and western blotting—Harvested cells were washed with PBS and lysed in RIPA buffer (50 mM Tris, 150 mM NaCl, 0.1% SDS, 0.5% sodium deoxycholate, 1% NP-40) supplemented with protease and phosphatase inhibitors. Protein concentration was quantified with the Pierce BCA Protein Assay Kit. Samples were mixed with 4x sample loading buffer and incubated for 5 min at 95°C. 30 μg of total protein lysate was resolved on SDS polyacrylamide gel according to standard procedure at 20 mA per gel and blotted onto a nitrocellulose membrane 0.45 μm (GE Healthcare) *via* Mini Trans-blot module (Bio-Rad) at a constant voltage (100 V) for 2 h. After blocking with 5% non-fat milk (Serva)/Tris-buffered saline with 0.05% Tween 20 (TBS-T) for 1 h, the membrane was incubated overnight in 5% bovine serum albumin (Sigma)/TBS-T with primary antibody against MPC1 (cell signaling 1:1000), MPC2 (cell signaling 1:1000), MCT4 (abcam 1:1000) and α-Tubulin (cell signaling 1:5000). Next day, the membrane was washed with TBS-T and incubated with corresponding fluorophore conjugated secondary antibody (Rockland

Immunochemical, 1:10000) in 1% non-fat milk/TBS-T for 1 h. The membrane was then washed again with TBS-T and fluorescence was assessed with Odyssey CLx imaging system (LI-COR Biosciences).

Gene expression analysis—Total RNA from ventricular tissue was isolated using RNeasy Mini kit (Qiagen), according to the manufacturer's instructions. cDNA synthesis was carried out using High Capacity cDNA Reverse Transcription Kit (ThermoFisher). SYBR Green-based real-time PCR was performed using a LightCycler 480 Real-Time PCR System (Roche). The housekeeping gene *RPL32* was used as an internal control for cDNA quantification and normalization of the amplified products. All data are reported as mean ± SEM.

Phalloidin staining—Differentiated H9c2 cells or primary adult cardiomyocytes were counted and seeded on micro cover glass slips (12 mm diameter) in appropriate media containing one of the following: vehicle (DMSO), UK-5099 (UK 10 μM), Phenylephrine (PE 100 μM) or VB124 (VB 20 μM). Cells were treated with drugs for indicated period of time. Subsequently, medium was removed and coverslips with cells were washed with PBS and fixed with 4% paraformaldehyde in PBS for 20 min at RT. Cells were washed again with PBS, permeabilized with 0.2% TritonX-100 for 10 min at RT, washed with PBS and blocked with 10% bovine serum albumin in PBS for 1 h at RT. After blocking, cells were washed with PBS, incubated in phalloidin conjugated with Alexa Fluor 488 (1:40 in PBS) and mounted on glass slides using mounting medium with DAPI (P36962, Thermo Scientific). Fluorescence images were taken by Zeiss Axio Observer Z1 microscope. The size of individual cells was quantified by ImageJ software (NIH). Images are representative of n≥15 images from four independent experiments for each condition.

Histology—Hearts were fixed with 4 % paraformaldehyde in PBS for 4 hours and in 10 % sucrose overnight, embedded in OCT and cut into 3–5 μM thick sections. Sections were processed with Hematoxylin and Eosin staining according to manufacturer's instructions. Stained sections were scanned at 0.63x magnification on Olympus SZX10 microscope.

Mouse RNA-Sequencing—RNA was isolated from murine ventricular tissue samples using the miRNeasyMini Kit (Qiagen). Total RNA samples (100–500 ng) were hybridized with Ribo-Zero Gold (Illumina) to substantially deplete cytoplasmic and mitochondrial rRNA from the samples. Stranded RNA sequencing libraries were prepared as described using the Illumina TruSeq Stranded Total RNA Library Prep Gold kit (20020598) with TruSeq RNA UD Indexes (20022371). Purified libraries were qualified on an Agilent Technologies 2200 TapeStation using a D1000 ScreenTape assay (cat# 5067–5582 and 5067–5583). The molarity of adapter-modified molecules was defined by quantitative PCR using the Kapa Biosystems Kapa Library Quant Kit (cat#KK4824). Individual libraries were normalized to 1.30 nM in preparation for Illumina sequence analysis. Sequencing libraries (1.3 nM) were chemically denatured and applied to an Illumina NovaSeq flow cell using the NovaSeq XP chemistry workflow (20021664). Following transfer of the flowcell to an Illumina NovaSeq instrument, a 2 × 51 cycle paired end sequence run was performed using a NovaSeq S1 reagent Kit (20027465).

RNA-seq analysis and bioinformatics—RNA-seq analysis was conducted with the High-Throughput Genomics and Bioinformatic Analysis Shared Resource at Huntsman Cancer Institute at the University of Utah. The mouse GRCm38 FASTA and GTF files were downloaded from Ensembl release 96 and the reference database was created using STAR version 2.7.0f with splice junctions optimized for 50 base-pair reads (Dobin et al., 2013). Optical duplicates were removed from the paired end FASTQ files using BBMap's Clumpify utility (v38.34) (https://sourceforge.net/projects/bbmap) and reads were trimmed of adapters using cutadapt 1.16 (Martin, 2011). The trimmed reads were aligned to the reference database using STAR in two-pass mode to output a BAM file sorted by coordinates. Mapped reads were assigned to annotated genes in the GTF file using featureCounts version 1.6.3 (Liao et al., 2014). The output files from cutadapt, FastQC, Picard CollectRnaSeqMetrics, STAR, and featureCounts were summarized using MultiQC to check for any sample outliers (Ewels et al., 2016). Differentially expressed genes with at least 95 read counts across all samples for a given time point (8wks or 16wks) were identified using DESeq2 version 1.24.0 (Love et al., 2014). Genes were then filtered using the criteria: FDR < 0.01, absolute log2 fold change >0.6, (Fold change > 1.516). Up- and down-regulated gene sets from each time point were then analyzed for enriched GO terms using Gprofiler (Reimand et al., 2007) with a Benjamini-Hochberg (Benjamini and Hochberg, 1995) FDR *p*-value correction thresholded at < 0.01. RNA-seq read counts were RPKM normalized for heatmap generation. Heatmaps were generated by gene-standardizing the RPKM gene values (mean = 0, stdev = 1) and plotting using XPRESSplot v0.2.2 (Berg et al., 2020), Matplotlib (Hunter, 2007), and Seaborn (https://github.com/mwaskom/seaborn).

Transmission electron microscopy and mitochondria volume density analysis —Cardiac tissue samples were fixed in 2.5% glutaraldehyde, 1% paraformaldehyde, in 0.1M sodium Cacodylate buffer. Fixation was performed overnight at 4°C. After washing in the same buffer, tissues were post-fixed for 2 hours in 2% Osmium Tetroxide buffered with cacodylate buffer, rinsed for 5 min in filtered nanopure water and stained with enbloc stain in Uranyl Acetate for 1 hour at room temperature. Following the post-staining, the tissues were dehydrated through a graded series of ethanol: 1× 10 min 50%, 1× 10 min 70%, 2× 10 min 95%, 4× 10 min in absolute ethanol and 3× 10 min with absolute acetone.

Infiltration was performed by incubating the specimens at room temperature in a gradually increasing concentration of Epoxy resin (Electron Microscopy Science Inc, Hatfield, PA). Specimens were transferred in 50% resin in acetone for 1 h and 75% resin with acetone for overnight. Following day, specimens were transferred to 100% resin for 8 h with 3 changes with fresh resin and embedded and polymerized at 60°C for 48 h. Ultrathin sections (70 nm) were obtained with diamond knife (Diatome) using Leica UC 6 (Leica Microsystems, Vienna, Austria), and post-stained for 10 min with saturated uranyl acetate and for 5 min with Reinold stain. Sections were imaged at 120 kV with JEOL 1400 Plus.

The mitochondrial volume density, defined as the volume occupied by mitochondria divided by the volume occupied by the cytoplasm, was estimated using stereology. as follows. A 10 × 10 square grid (10 × 10 chosen for ease of use with Adobe Photoshop was overlaid on each image loaded in Adobe Photoshop and mitochondria lying under intercepts were counted. The relative volume occupied by mitochondria was expressed as the ratio of

intercepts coinciding with mitochondria relative to the total number of intercepts. Intermitochondrial junctions were determined using the point counting method (Weibel et al., 1966).

Metabolomic analysis—The levels of metabolites in the cardiac tissue were measured by gas chromatography–mass spectroscopy (GC-MS) analysis. A 30 mg of tissue was carefully weighed and placed into a bead mill tube containing 1.4 mm ceramic beads (MoBio Laboratories, Carlsbad, CA). To this tube was added 30 μL of 90% MeOH (aq) that had been chilled to −20°C. Using an Omni Bead Ruptor 24 bead mill (Omni-Inc, Kennesaw, GA) the tissue was homogenized for 30 seconds at 6.5m/sec. The ruptured tissue was incubated for one hour at −20°C to precipitate protein. Following incubation cell debris was removed by centrifugation, 14000 × g for 5 minutes at 4°C. The supernatant was then transferred to microfuge tubes and the solvent removed en vacuo. All GC-MS analysis was performed with a Waters GCT Premier mass spectrometer fitted with an Agilent 6890 gas chromatograph and a Gerstel MPS2 autosampler. Dried samples were suspended in 40 μL of a 40 mg/mL O-methoxylamine hydrochloride (MOX) in pyridine and incubated for one hour at 30°C. 10 μL of N-methyl-N-trimethylsilyltrifluoracetamide (MSTFA) was added automatically via the autosampler and incubated for 60 minutes at 37°C with shaking. After incubation 3 μL of a fatty acid methyl ester standard solution was added via the autosampler. Then 1 μL of the prepared sample was injected to the gas chromatograph inlet in the split mode with the inlet temperature held at 250°C. A 10:1 split ratio was used for analysis. The gas chromatograph had an initial temperature of 95°C for one minute followed by a 40°C/min ramp to 110°C and a hold time of 2 minutes. This was followed by a second 5°C/min ramp to 250°C, a third ramp to 350°C, then a final hold time of 3 minutes. A 30 m Phenomex ZB5–5 MSi column with a 5 m long guard column was employed for chromatographic separation. Helium was used as the carrier gas at 1 mL/min. Data was extracted from each chromatogram as area under the curve for individual metabolites. Each sample was first normalized to the added standard d4-succinate to account for extraction efficiency followed by normalization to tissue weight. Due to this being a broad scope metabolomics analysis, no normalization for ionization efficiency or concentration standards was performed.

Metabolite Extraction—The procedures for metabolite extraction from cultured cells are described in previous studies (Cluntun et al., 2015, Lukey et al., 2019). Briefly, adherent cells were grown in 10 cm plates in biological triplicate to 80% confluence, medium was rapidly aspirated and cells were washed with cold PBS on ice. Then, 3 mL of extraction solvent (80% methanol/water) cooled to −80°C was added to each well, and the dishes were transferred to −80°C for 15 min. Cells were then scraped into the extraction solvent on dry ice. All metabolite extracts were centrifuged at 20,000 Relative Centrifugal Force (RCF) at 4°C for 10 min. Each sample was then transferred to a new 1.5 mL tube. Finally, the solvent in each sample was evaporated in a Speed Vacuum, and stored at −80°C until they were run on the mass spec.

[U-$^{13}C_6$]-Glucose Labeling—Cells were grown to 80% confluence in 10 cm plates with standard culture medium and washed with sterile PBS. Then, culture medium in which

glucose was replaced by [$^{13}C_6$]-L-glucose (Cambridge Isotope Laboratories), supplemented with dialyzed Fetal Bovine Serum (GIBCO) and appropriate concentrations of inhibitors were added (5 ml/well), and incubated for 4 h. Metabolites were extracted as described above. Data was corrected for naturally occurring ^{13}C isotope abundance before analysis as described in (Buescher et al., 2015).

General Synthetic Methods—All reactions were performed in flame-dried or oven-dried glassware under a positive pressure of dry nitrogen or dry argon and were stirred magnetically unless otherwise indicated. All solvents and chemicals were purchased from standard commercial vendors and used as received unless otherwise noted. Yields are not optimized. The chemical names were generated using the Symyx Draw 3.1 chemical drawing program, available from MDL Information Systems, a division of Symyx technologies, Inc. (Santa Clara, CA). Reactions were monitored by TLC (thin layer chromatography) using 0.25 mm silica gel 60F254 plates purchased from EMD chemicals (Norwood, OH). Purification was performed with Teledyne ISCO CombiFlash Rf (Lincoln, NE). ^1H NMR spectra were recorded on Varian Mercury 400 MHz instrument. Proton chemical shifts are expressed in parts per million (ppm) relative to TMS and calibrated using residual undeuterated solvent as internal reference. Compound purity was determined by an Agilent HP1050 instrument with 4.6 mm × 150 mm XTerra MS C18 3.5 μm column and Upchurch 5 μm precolumn 24 × 12mm. The flow rate was 1.2 mL/min, and the injection volume was 5 μL. HPLC conditions were as follows: mobile phase A, HPLC grade water (0.1%TFA); mobile phase B, HPLC grade acetonitrile (0.1%TFA); UV detector, 250 nm; 95%A/5%B to 0%A/100%B in 10 min, 100% B in 10–11 min, 100%B to 95%A/5% B in 11–13 min, 95%A/5% B in 13–15 min.

Synthesis of VB124—Step 1. Into a 50-mL round-bottom flask, was placed a solution of methyl 4-(3-cyclopropoxyphenyl)-2,4-dioxobutanoate (1 g, 3.81 mmol, 1.00 equiv) in acetic acid (30 mL). This was followed by the addition of (2-chlorophenyl)hydrazine dihydrochloride (817 mg, 3.79 mmol, 1.00 equiv), in portions at room temperature. The resulting solution was stirred for 2 h at 100°C in an oil bath. The resulting mixture was concentrated under vacuum. The resulting solution was diluted with 200 mL of EA. The pH value of the solution was adjusted to 7–8 with (sat)NaHCO3(aq). The mixture was dried over anhydrous sodium sulfate and concentrated under vacuum. The residue was applied onto a silica gel column with ethyl acetate/petroleum ether (1:4). This resulted in 1.3 g (92%) of methyl 1-(2-chlorophenyl)-5-(3-cyclopropoxyphenyl)-1H-pyrazole-3-carboxylate as a yellow solid.

Step 2. Into a 50-mL round-bottom flask, was placed a solution of methyl 1-(2-chlorophenyl)-5-(3-cyclopropoxyphenyl)-1H-pyrazole-3-carboxylate (1.3 g, 3.52 mmol, 1.00 equiv) in tetrahydrofuran (30 mL). This was followed by the addition of LiBH4 (5.3 mL, 3.00 equiv) dropwise with stirring at 0°C. The resulting solution was stirred for 16 h at room temperature. The reaction was then quenched by the addition of water/ice. The resulting solution was extracted with 200 mL of ethyl acetate and the organic layers combined and dried over anhydrous sodium sulfate and concentrated under vacuum. The residue was applied onto a silica gel column with ethyl acetate/petroleum ether (3:10). This

resulted in 1.0 g (83%) of [1-(2-chlorophenyl)-5-(3-cyclopropoxyphenyl)-1H-pyrazol-3-yl] methanol as yellow oil.

Step 3. Into a 100-mL round-bottom flask, was placed a solution of [1-(2-chlorophenyl)-5-(3-cyclopropoxyphenyl)-1H-pyrazol-3-yl] methanol (1.0 g, 2.93 mmol, 1.00 equiv) in dichloromethane (50 mL), CBr4 (1.96 g, 5.87 mmol, 2.00 equiv). This was followed by the addition of PPH3 (1.54 g, 5.87 mmol, 2.00 equiv), in portions at 0°C. The resulting solution was stirred for 2 h at room temperature. The resulting mixture was concentrated under vacuum. The residue was applied onto a silica gel column with ethyl acetate/petroleum ether (1:5). This resulted in 1.1 g (93%) of 3-(bromomethyl)-1-(2-chlorophenyl)-5-(3-cyclopropoxyphenyl)-1H-pyrazole as yellow oil.

Step 4. Into a 25-mL round-bottom flask, was placed a solution of methyl 2-hydroxy-2-methylpropanoate (264 mg, 2.23 mmol, 3.00 equiv) in tetrahydrofuran (10 mL). This was followed by the addition of sodium hydride (90 mg, 3.75 mmol, 3.00 equiv), in portions at 0°C. To this was added 3-(bromomethyl)-1-(2-chlorophenyl)-5-(3-cyclopropoxyphenyl)-1H-pyrazole (300 mg, 0.74 mmol, 1.00 equiv) at 0°C. The resulting solution was stirred for 16 h at room temperature. The reaction was then quenched by the addition of water/ice. The resulting solution was extracted with 100 mL of ethyl acetate and the organic layers combined. The resulting mixture was washed with 2× 100 mL of Brine. The mixture was dried over anhydrous sodium sulfate and concentrated under vacuum. The residue was applied onto a Prep-TLC with ethyl acetate/petroleum ether (1:2). This resulted in 120 mg (37%) of methyl 2-[[1-(2-chlorophenyl)-5-(3-cyclopropoxyphenyl)-1H-pyrazol-3-yl] methoxy]-2-methylpropanoate as a yellow solid.

Step 5. Into a 25-mL round-bottom flask, was placed a solution of methyl 2-[[1-(2-chlorophenyl)-5-(3-cyclopropoxyphenyl)-1H-pyrazol-3-yl] methoxy]-2-methylpropanoate (120 mg, 0.27 mmol, 1.00 equiv) in tetrahydrofuran/H2O (8/4 mL). This was followed by the addition of LiOH (39 mg, 1.63 mmol, 6.00 equiv), in portions at room temperature. The resulting solution was stirred for 2 h at room temperature. The pH value of the solution was adjusted to 3–4 with (con)HCl. The resulting solution was extracted with 100 mL of ethyl acetate and the organic layers combined. The resulting mixture was washed with 1 × 50 mL of brine. The mixture was dried over anhydrous sodium sulfate. The resulting mixture was concentrated under vacuum. The residue was purified by Prep-HPLC with following conditions: Column: SunFire Prep C18 OBD Column 19mm × 150mm 5μm 10nm; Mobile Phase A: Water(0.1%FA), Mobile Phase B: ACN; Flow rate: 18 mL/min; Gradient: 69% B to 71% B in 8 min; 254 nm; Rt: 7.0 min. This resulted in 54.3 mg (47%) of 2-[[1-(2-chlorophenyl)-5-(3-cyclopropoxyphenyl)-1H-pyrazol-3-yl]methoxy]-2-methylpropanoic acid as colorless oil. LC-MS-PH-VET-95–0: (ES, *m/z*): 427 ^{1}H-NMR: (MeOD, *ppm*): δ: 0.50 – 0.59 (m, 2H), 0.63 – 0.72 (m, 2H), 1.55 (s, 6H), 3.53 (tt, 1H), 4.63 (s, 2H), 6.73 (s, 1H), 6.86 – 6.98 (m, 3H), 7.22 (t, 1H), 7.41 – 7.61 (m, 4H).

MCT4 and MCT1 Fluorescence-Based Activity Assays—MCT4 and MCT1 lactate transport assays that use the pH-sensitive fluorescent dye 2′−7′-*bis*(carboxyethyl)-5(6)-carboxyfluorescein (BCECF) to detect changes in intracellular pH (pH_i) accompanying MCT-mediated lactate/proton symport, were developed in a manner similar to that reported

previously (Murray et al., 2005). To obtain BCECF-loaded cells, ~7 million trypsinized (0.05% Trypsin-EDTA) cells were pelleted (300 × g, 1 minute) and resuspended in 1 mL HEPES-buffered Tyrode's Solution (119 mM NaCl, 5 mM KCl, 25 mM HEPES buffer, 2 mM $CaCl_2$, 2 mM $MgCl_2$, 6 g/L D-glucose, pH adjusted to 7.4). Cells were re-pelleted (300 × g, 1 minute) and resuspended in 0.5 mL HEPES-buffered Tyrode's Solution. To this was added 2 μL of BCECF-AM ester (Fisher Scientific, Hampton, NH, USA) (30 mM stock solution in DMSO), and the reaction was incubated at 37°C for 5 minutes. Cells were again pelleted (300 × g, 1 minute), washed twice with 1 mL HEPES-buffered Tyrode's Solution, then resuspended in 0.5 mL HEPES-buffered Tyrode's Solution. To measure lactate import, 2.5 μL BCECF-loaded cells, along with either 10 μL DMSO or 100x compound in DMSO, were added to 937.5 μL of Tyrode's Solution in a quartz 1.0 mL cuvette (B0631116, PerkinElmer, Waltham, MA, USA). Fluorescence measurements are performed on a PerkinElmer LS55 fluorescence spectrometer with dual excitation wavelengths achieved using a filter wheel (FL Winlab program: Fast Filter; Excitation 490/440; Emission 535). After establishing baseline BCECF fluorescence (around 10–20 s), 50 μL of 1 M sodium L-lactate (Sigma-Aldrich, St. Louis, MO, USA) was added to the cuvette (final concentration: 50 mM) and rapidly mixed. The time-dependent decrease in BCECF fluorescence (490/440 ratio) was fit to an exponential decay curve (Prism GraphPad, San Diego, CA, USA) to determine the rate of lactate transport. Lactate export was measured similarly to import. Here, however, 2.5 μL BCECF-loaded cells were added to 937.5 μL of Tyrode's Solution and 50 μL of 1 M sodium L-lactate, followed after 2 minutes by either 10 μL DMSO or 100x compound in DMSO. Cells were pelleted (300 × g, 1 minute) followed by resuspension in 990 μL of Tyrode's Solution + either 10 μL DMSO or 100x compound in DMSO, and immediate fluorescence measurement as above.

CRISPR-Based Synthetic Lethality Screen—To construct a Cas9 expressing MDA-MB-231 cell line, MDA-MB-231 cells were transduced with lentiCas9-Blast (Addgene catalog #: 52962-LV, Watertown, MA, USA) and then selected with 1 μg/mL blasticidin for 9 days. Single cells were then plated in individual wells of a 96-well plate and left undisturbed for 13 days. Colonies formed by expansion of single cells for 13 days, Cas9 expression was determined by Western blotting, and a single clone was chosen for the screening based on Cas9/β-actin ratio.

A human CRISPR knockout pooled library (Brunello, Addgene Catalog #73178-LV, Watertown, MA, USA) consisting of 76,441 sgRNAs targeting 19,114 genes and 1000 nontargeting controls in the lentiCRISPRv2 lentivirus plasmid was used to infect Cas9-expressing MDA-MB-231 cells.

The level of lentiviral titer for MDA-MB-231 cells was determined through transduction. For each lentivirus, 5 wells of a 12-well plate were seeded at a density of 3×10^6 cells in 2 ml RPMI medium per well with 8 μg/ml of polybrene. Into each well was added 100μl, 40 μl, 20 μl, 10 μl, or 0 μl of lentivirus supernatant. (2) Cells were spinfected by centrifuging the plates at 1000 × g for 30 min at room temperature, followed by return to incubator. (3) Spinfections were replated for calculation of viral titer. 24 h after the end of spinfection, medium was removed and cells gently washed with 400 μl TrypLE per well, followed by addition of 100 μl TrypLE, and incubated at 37°C for 5 min to dissociate the cells. 2 mL of

RMPI medium was added per well and cells were resuspended by pipetting up and down. (4) For each virus condition, 2 wells of a 96-well clear bottom black tissue culture plate were seeded at a density of 4×10^5 cells with or without puromycin (2μg/ml). (5) 72 h after replating, when the no virus conditions contained no viable cells and the no antibiotic selection conditions were at 80–90% confluency, cell numbers for each condition were quantified. For each virus condition, the multiplicity of infection (MOI) was calculated as the cell numbers of the condition with puromycin divided by the condition without antibiotic selection. A linear relationship between lentivirus supernatant volume and MOI was expected at lower volumes, with saturation achieved at higher volumes.

To ensure that most cells receive only one genetic perturbation, the sgRNA library was transduced at an MOI < 0.3. After the appropriate selection for 7 days, the cells were ready for screening. (1) Cells were seeded in 12-well plates at a density of 3×10^6 cells in 2 mL RPMI medium per well with 8 μg/ml of polybrene. 40μl of lentivirus supernatant (MOI: 0.3) was added to each well followed by thorough mixing by pipetting up and down. Cells were spinfected by spinning the plates at 1000 × g for 1.5 h at room temperature followed by return to incubator. (2) 24 h after the end of spinfection, media was removed, and cells gently washed with 400 μl TrypLE per well, followed by addition 100 μl of TrypLE, and incubation at 37°C for 5 min to dissociate the cells. To each well, 2 ml of RMPI media was added with the appropriate selection antibiotic (2 ug/ml puromycin) for the lentivirus and cells were resuspended by pipetting up and down. The resuspended cells were pooled, centrifuged at 1000 × g for 5 mins, then resuspended and seeded into T150 flasks (4 wells/flask) in 50 ml of RPMI medium with selection antibiotic. (3) Media was refreshed with selection antibiotic every 3 days and passaged for 7 days to ensure death of uninfected cells. (4) At the end of selection, cells were split into four experimental samples (2 DMSO controls, 2 VB124). Each sample had 3.06×10^7 cells in 4x T175 or 3x T225 flask (each T175 yields 8×10^6 cells, while each T225 yields 1.2×10^7 cells). Cells were passaged every 3 or 4 days for 3 weeks.

At the end of the screen, genomic DNA was (gDNA) was harvested from at least 3.06×10^7 cells to maintain a coverage of 400 using QIAamp® DNA Blood Maxi kit according to the manufacturer's protocol (Qiagen, Germantown, MD, USA). Water was used to elute the gDNA. Frozen cell pellets or isolated gDNA were stored at −20°C.

PCR was designed to enrich (amplify) sgRNAs. During the enrichment, Illumina 5′ and Illumina 3′ adapters are added to the 3′ and 5′ end of the sgRNA cassette, and the index (barcode for de-multiplexing) was also added to one end. Below is a cartoon depicting the reaction, followed by sequences of the primers. After the reaction was complete, PCR reactions were pooled, separated on a 2% (wt/vol) agarose gel, (successful reactions should yield a ~245bp product), and the PCR product purified by using the QIAquick PCR purification kit according to the manufacturer's directions (Qiagen, Germantown, MD, USA) Gel-extracted samples were quantified using the Qubit dsDNA HS Assay (Thermo Fisher, Waltham MA, USA). Samples were sequenced on the Illumina HiSeq with 18% PhiX control (Illumina, San Diego, CA, USA).

Osmotic minipump model—12 weeks old C57BL/6 mice were divided into 4 groups, weighted, and screened before surgery via echocardiography to establish their baseline. Surgical instruments were sterilized using a glass bead sterilizer prior to the surgery and aseptic technique was utilized during the procedure. The osmotic minipumps (Alzet, model 2004) were filled with isoproterenol in 0.9% NaCl (30mg/kg/day for 28 days) according to manufacturer instructions. The pumps were inserted subcutaneously in the back through small subsequently sutured incision, under isoflurane (1.5% in O_2) anesthesia. The mice were given VB124 dissolved in 0.5% methylcellulose and 0.1% Tween-20 by oral gavage every day (30mg/kg/day in 200 μL) for 28 days. Mice were screened by echocardiography and weighted every week. After 28 days of treatment, the mice were sacrificed by cervical dislocation and blood and heart tissue was taken for further analysis.

Mitochondrial membrane potential microscopy and quantification—Live cardiomyocytes were labeled with 100 nM MitoTracker Red CMXROS and 200 nM MitoTracker Green. Cells were plated in laminin coated chambered coverglass (Fisher, 155409). Cells were pretreated with DMSO (Veh), Isoproterenol, or Isoproterenol + VB124 for 24 h. Cells were then incubated with dyes for 30 minutes at 37°C in a humidified incubator with 5% CO_2, then washed twice with PBS and replaced with fresh media. Cells were then imaged using a Zeiss AxioObserver Z1 fluorescence microscope (Carl Zeiss) equipped with 40x oil-immersion objective. Digital fluorescence and differential interference contrast (DIC) images were acquired using a monochrome digital camera (AxioCam 506, Carl Zeiss). Images were exported from Zeiss Zen software package and analyzed for fluorescence intensity using FiJi ImageJ. Images are representative of n≥30 images from three independent experiments.

ROS determination—To determine ROS levels in cardiomyocytes, live cardiomyocytes were labeled with CM-H_2DCFDA. Cells were plated in laminin coated chambered cover glass (Fisher, 155409). Cells were pretreated with DMSO (Veh), H_2O_2, Isoproterenol, or Isoproterenol + VB124 for 24 h. Cells were then incubated with 5μM of the dye for 20 minutes at 37°C in a humidified incubator with 5% CO_2, then washed twice with PBS and replaced with fresh media. Cells were then imaged using a Zeiss AxioObserver Z1 fluorescence microscope (Carl Zeiss) equipped with 40x oil-immersion objective. Digital fluorescence and differential interference contrast (DIC) images were acquired using a monochrome digital camera (AxioCam 506, Carl Zeiss). Images were exported from Zeiss Zen software package and analyzed for fluorescence intensity using FiJi ImageJ. Images are representative of n≥30 images from three independent experiments.

Cardiomyocyte Imaging—Cardiomyocytes were isolated from the adult mouse heart as described above. Cells were stored in the physiological ringer's solution and imaged using Leica SP8 confocal microscope. Images were acquired using 488 excitation wavelength with a pinhole size = 1AU and a transillumination detector (TLD). All images were taken using 10x lens. Cell length and width were calculated using ImageJ software and statistical analysis was performed using GraphPad Prism. Images are representative of n≥15 images from four independent experiments.

Echocardiographic analysis—Mice were anesthetized with 1.5% Isoflurane (Vet One, NDC 13985-046-60) during echocardiography. Echocardiographic images were taken on Vivo system. Echocardiography was performed serially. 2D long-axis and short-axis views were obtained and used for analysis using the vivo strain software (version 3.1.1). Two consecutive cardiac cycles were used for all the measurements. Limb leads were present in the imaging set-up and the mice limbs were taped to it with a conductive cream to record electrocardiogram (ECG).

QUANTIFICATION AND STATISTICAL ANALYSIS

The statistical details of experiments can be found in the figure legends. All data expressed as mean ± SEM unless otherwise indicated. Student's t test was used for 2 group comparison. One-Way ANOVA and Sidak's comparisons were used for multigroup comparison. Log-rank test and Wilcoxon test were used for survival curve comparison. *p*-values less than 0.05 were considered statistically significant. Statistical analyses and graphics were carried out with GraphPad Prism 8 software and Microsoft Excel.

Supplementary Material

Refer to Web version on PubMed Central for supplementary material.

Acknowledgements

We thank Donor Connect (https://www.donorconnect.life/) for facilitating the work of our research team members acquiring the non-failing donor control hearts in the operating rooms of several hospitals of the Intermountain West. We also thank Drs. David Sabatini, Chris Stubben and Ms. Linda Nikolova for reagents, technical assistance, data analysis and advice. We also thank members of the Rutter and Drakos labs for helpful discussions. We acknowledge the following for funding: CA228346 and R35GM131854 to J.R.; R01HL135121 and R01HL132067 to S.G.D.; 1S10OD016232-01, 1S10OD018210-01A1, 1S10OD021505-01, and U54DK110858 to J.E.C.; R00CA215307 to G.S.D.; R01DK108833 and R01DK112826 to W.L.H.; The Thoracic Surgery Foundation, The American Association for Thoracic Surgery Graham Foundation and The American College of Surgeons for S.H.M.; the Nora Eccles Treadwell Foundation to S.G.D. and J.R.; the AHA Heart Failure Strategically Focused Research Network 16SFRN29020000 to S.G.D.; 5T32HL007576-33 to A.A.C.; 19POST34381084 to R.B., 5T32DK091317 to C.N.C; 1T32DK11096601 and 1F99CA253744 to J.A.B.; and 5K00CA212445 to A.J.B.. J.R. is an investigator of the Howard Hughes Medical Institute. The content of this manuscript is solely the responsibility of the authors and does not necessarily represent the official views of the National Institutes of Health (NIH).

References

ABEL ED & DOENST T 2011. Mitochondrial adaptations to physiological vs. pathological cardiac hypertrophy. Cardiovasc Res, 90, 234–42. [PubMed: 21257612]

ACIN-PEREZ R, LECHUGA-VIECO AV, DEL MAR MUNOZ M, NIETO-ARELLANO R, TORROJA C, SANCHEZ-CABO F, JIMENEZ C, GONZALEZ-GUERRA A, CARRASCOSO I, BENINCA C, QUIROS PM, LOPEZ-OTIN C, CASTELLANO JM, RUIZ-CABELLO J, JIMENEZ-BORREGUERO LJ & ENRIQUEZ JA 2018. Ablation of the stress protease OMA1 protects against heart failure in mice. Sci Transl Med, 10.

ALLARD MF, SCHONEKESS BO, HENNING SL, ENGLISH DR & LOPASCHUK GD 1994. Contribution of oxidative metabolism and glycolysis to ATP production in hypertrophied hearts. Am J Physiol, 267, H742–50. [PubMed: 8067430]

BADOLIA R, RAMADURAI DKA, ABEL ED, FERRIN P, TALEB I, SHANKAR TS, KROKIDI AT, NAVANKASATTUSAS S, MCKELLAR SH, YIN M, KFOURY AG, WEVER-PINZON O, FANG JC, SELZMAN CH, CHAUDHURI D, RUTTER J & DRAKOS SG 2020. The Role of Nonglycolytic Glucose Metabolism in Myocardial Recovery Upon Mechanical Unloading and Circulatory Support in Chronic Heart Failure. Circulation, 142, 259–274. [PubMed: 32351122]

BARGER PM & KELLY DP 1999. Fatty acid utilization in the hypertrophied and failing heart: molecular regulatory mechanisms. Am J Med Sci, 318, 36–42. [PubMed: 10408759]

BARTH E, STAMMLER G, SPEISER B & SCHAPER J 1992. Ultrastructural quantitation of mitochondria and myofilaments in cardiac muscle from 10 different animal species including man. J Mol Cell Cardiol, 24, 669–81. [PubMed: 1404407]

BEKFANI T, WESTPHAL F & SCHULZE PC 2018. Therapeutic options in advanced heart failure. Clin Res Cardiol, 107, 114–119. [PubMed: 29987596]

BENJAMIN D, ROBAY D, HINDUPUR SK, POHLMANN J, COLOMBI M, EL-SHEMERLY MY, MAIRA SM, MORONI C, LANE HA & HALL MN 2018. Dual Inhibition of the Lactate Transporters MCT1 and MCT4 Is Synthetic Lethal with Metformin due to NAD+ Depletion in Cancer Cells. Cell Rep, 25, 3047–3058 e4. [PubMed: 30540938]

BENJAMINI Y & HOCHBERG Y 1995. Controlling the False Discovery Rate: A Practical and Powerful Approach to Multiple Testing. Journal of the Royal Statistical Society. Series B (Methodological), 57, 289–300.

BENSARD CL, WISIDAGAMA DR, OLSON KA, BERG JA, KRAH NM, SCHELL JC, NOWINSKI SM, FOGARTY S, BOTT AJ, WEI P, DOVE KK, TANNER JM, PANIC V, CLUNTUN A, LETTLOVA S, EARL CS, NAMNATH DF, VAZQUEZ-ARREGUIN K, VILLANUEVA CJ, TANTIN D, MURTAUGH LC, EVASON KJ, DUCKER GS, THUMMEL CS & RUTTER J 2020. Regulation of Tumor Initiation by the Mitochondrial Pyruvate Carrier. Cell Metab, 31, 284–300 e7. [PubMed: 31813825]

BERG JA, BELYEU JR, MORGAN JT, OUYANG Y, BOTT AJ, QUINLAN AR, GERTZ J & RUTTER J 2020. XPRESSyourself: Enhancing, standardizing, and automating ribosome profiling computational analyses yields improved insight into data. PLoS Comput Biol, 16, e1007625. [PubMed: 32004313]

BERGMAN BC, TSVETKOVA T, LOWES B & WOLFEL EE 2009. Myocardial glucose and lactate metabolism during rest and atrial pacing in humans. J Physiol, 587, 2087–99. [PubMed: 19289551]

BERTERO E & MAACK C 2018. Metabolic remodelling in heart failure. Nat Rev Cardiol, 15, 457–470. [PubMed: 29915254]

BING RJ, SIEGEL A, VITALE A, BALBONI F, SPARKS E, TAESCHLER M, KLAPPER M & EDWARDS S 1953. Metabolic studies on the human heart in vivo. I. Studies on carbohydrate metabolism of the human heart. Am J Med, 15, 284–96. [PubMed: 13080276]

BIRKS EJ, GEORGE RS, HEDGER M, BAHRAMI T, WILTON P, BOWLES CT, WEBB C, BOUGARD R, AMRANI M, YACOUB MH, DREYFUS G & KHAGHANI A 2011. Reversal of severe heart failure with a continuous-flow left ventricular assist device and pharmacological therapy: a prospective study. Circulation, 123, 381–90. [PubMed: 21242487]

BIRKS EJ, TANSLEY PD, HARDY J, GEORGE RS, BOWLES CT, BURKE M, BANNER NR, KHAGHANI A & YACOUB MH 2006. Left ventricular assist device and drug therapy for the reversal of heart failure. N Engl J Med, 355, 1873–84. [PubMed: 17079761]

BIRSOY K, WANG T, CHEN WW, FREINKMAN E, ABU-REMAILEH M & SABATINI DM 2015. An Essential Role of the Mitochondrial Electron Transport Chain in Cell Proliferation Is to Enable Aspartate Synthesis. Cell, 162, 540–51. [PubMed: 26232224]

BISETTO S, WRIGHT MC, NOWAK RA, LEPORE AC, KHURANA TS, LORO E & PHILP NJ 2019. New Insights into the Lactate Shuttle: Role of MCT4 in the Modulation of the Exercise Capacity. iScience, 22, 507–518. [PubMed: 31837519]

BOEHMER JP, STARLING RC, COOPER LT, TORRE-AMIONE G, WITTSTEIN I, DEC GW, MARKHAM DW, ZUCKER MJ, GORCSAN J 3RD, MCTIERNAN C, KIP K, MCNAMARA DM & INVESTIGATORS I 2012. Left ventricular assist device support and myocardial recovery in recent onset cardiomyopathy. J Card Fail, 18, 755–61. [PubMed: 23040110]

BONEN A 2001. The expression of lactate transporters (MCT1 and MCT4) in heart and muscle. Eur J Appl Physiol, 86, 6–11. [PubMed: 11820324]

BRANCO AF, PEREIRA SP, GONZALEZ S, GUSEV O, RIZVANOV AA & OLIVEIRA PJ 2015. Gene Expression Profiling of H9c2 Myoblast Differentiation towards a Cardiac-Like Phenotype. PLoS One, 10, e0129303. [PubMed: 26121149]

BRICKER DK, TAYLOR EB, SCHELL JC, ORSAK T, BOUTRON A, CHEN YC, COX JE, CARDON CM, VAN VRANKEN JG, DEPHOURE N, REDIN C, BOUDINA S, GYGI SP, BRIVET M, THUMMEL CS & RUTTER J 2012. A mitochondrial pyruvate carrier required for pyruvate uptake in yeast, Drosophila, and humans. Science, 337, 96–100. [PubMed: 22628558]

BROWN DA, PERRY JB, ALLEN ME, SABBAH HN, STAUFFER BL, SHAIKH SR, CLELAND JG, COLUCCI WS, BUTLER J, VOORS AA, ANKER SD, PITT B, PIESKE B, FILIPPATOS G, GREENE SJ & GHEORGHIADE M 2017. Expert consensus document: Mitochondrial function as a therapeutic target in heart failure. Nat Rev Cardiol, 14, 238–250. [PubMed: 28004807]

BUESCHER JM, ANTONIEWICZ MR, BOROS LG, BURGESS SC, BRUNENGRABER H, CLISH CB, DEBERARDINIS RJ, FERON O, FREZZA C, GHESQUIERE B, GOTTLIEB E, HILLER K, JONES RG, KAMPHORST JJ, KIBBEY RG, KIMMELMAN AC, LOCASALE JW, LUNT SY, MADDOCKS OD, MALLOY C, METALLO CM, MEUILLET EJ, MUNGER J, NOH K, RABINOWITZ JD, RALSER M, SAUER U, STEPHANOPOULOS G, ST-PIERRE J, TENNANT DA, WITTMANN C, VANDER HEIDEN MG, VAZQUEZ A, VOUSDEN K, YOUNG JD, ZAMBONI N & FENDT SM 2015. A roadmap for interpreting (13)C metabolite labeling patterns from cells. Curr Opin Biotechnol, 34, 189–201. [PubMed: 25731751]

CHACINSKA A, KOEHLER CM, MILENKOVIC D, LITHGOW T & PFANNER N 2009. Importing mitochondrial proteins: machineries and mechanisms. Cell, 138, 628–44. [PubMed: 19703392]

CHEN WW, FREINKMAN E & SABATINI DM 2017. Rapid immunopurification of mitochondria for metabolite profiling and absolute quantification of matrix metabolites. Nat Protoc, 12, 2215–2231. [PubMed: 29532801]

CHEN WW, FREINKMAN E, WANG T, BIRSOY K & SABATINI DM 2016. Absolute Quantification of Matrix Metabolites Reveals the Dynamics of Mitochondrial Metabolism. Cell, 166, 1324–1337 e11. [PubMed: 27565352]

CHONG J, SOUFAN O, LI C, CARAUS I, LI S, BOURQUE, WISHART DS & XIA J 2018. MetaboAnalyst 4.0: towards more transparent and integrative metabolomics analysis. Nucleic Acids Res, 46, W486–W494. [PubMed: 29762782]

CLERK A & SUGDEN PH 1999. Activation of protein kinase cascades in the heart by hypertrophic G protein-coupled receptor agonists. Am J Cardiol, 83, 64H–69H.

CLUNTUN AA, HUANG H, DAI L, LIU X, ZHAO Y & LOCASALE JW 2015. The rate of glycolysis quantitatively mediates specific histone acetylation sites. Cancer Metab, 3, 10. [PubMed: 26401273]

CRESTI A, CHIAVARELLI M, GLAUBER M, TANGANELLI P, SCALESE M, CESAREO F, GUERRINI F, CAPATI E, FOCARDI M & SEVERI S 2016. Incidence rate of primary cardiac tumors: a 14-year population study. J Cardiovasc Med (Hagerstown), 17, 37–43. [PubMed: 25022931]

DAI C, LI Q, MAY HI, LI, ZHANG, SHARMA, SHERRY AD, MALLOY CR, KHEMTONG C, ZHANG Y, DENG Y, GILLETTE TG, XU J, SCADDEN DT & WANG ZV 2020. Lactate Dehydrogenase A Governs Cardiac Hypertrophic Growth in Response to Hemodynamic Stress. Cell Rep, 32, 108087. [PubMed: 32877669]

DANDEL M, WENG Y, SINIAWSKI H, POTAPOV E, DREWS T, LEHMKUHL HB, KNOSALLA C & HETZER R 2008. Prediction of cardiac stability after weaning from left ventricular assist devices in patients with idiopathic dilated cardiomyopathy. Circulation, 118, S94–105. [PubMed: 18824777]

DE GROOT MJ, VAN HELDEN MA, DE JONG YF, COUMANS WA & VAN DER VUSSE GJ 1995. The influence of lactate, pyruvate and glucose as exogenous substrates on free radical defense mechanisms in isolated rat hearts during ischaemia and reperfusion. Mol Cell Biochem, 146, 147–55. [PubMed: 7565644]

DELL'ANNO I, BARONE E, MUTTI L, RASSL DM, MARCINIAK SJ, SILVESTRI R, LANDI S & GEMIGNANI F 2020. Tissue expression of lactate transporters (MCT1 and MCT4) and prognosis of malignant pleural mesothelioma (brief report). J Transl Med, 18, 341. [PubMed: 32887638]

DIAKOS NA, NAVANKASATTUSAS S, ABEL ED, RUTTER J, MCCREATH L, FERRIN P, MCKELLAR SH, MILLER DV, PARK SY, RICHARDSON RS, DEBERARDINIS R, COX JE, KFOURY AG, SELZMAN CH, STEHLIK J, FANG JC, LI DY & DRAKOS SG 2016. Evidence of Glycolysis Up-Regulation and Pyruvate Mitochondrial Oxidation Mismatch During Mechanical

Unloading of the Failing Human Heart: Implications for Cardiac Reloading and Conditioning. JACC Basic Transl Sci, 1, 432–444. [PubMed: 28497127]

DOBIN A, DAVIS CA, SCHLESINGER F, DRENKOW J, ZALESKI C, JHA S, BATUT P, CHAISSON M & GINGERAS TR 2013. STAR: ultrafast universal RNA-seq aligner. Bioinformatics, 29, 15–21. [PubMed: 23104886]

DRAKOS SG, PAGANI FD, LUNDBERG MS & BALDWIN JT 2017. Advancing the Science of Myocardial Recovery With Mechanical Circulatory Support: A Working Group of the National, Heart, Lung, and Blood Institute. JACC Basic Transl Sci, 2, 335–340. [PubMed: 28736756]

DRAKOS SG, WEVER-PINZON O, SELZMAN CH, GILBERT EM, ALHARETHI R, REID BB, SAIDI A, DIAKOS NA, STOKER S, DAVIS ES, MOVSESIAN M, LI DY, STEHLIK J, KFOURY AG & INVESTIGATORS U 2013. Magnitude and time course of changes induced by continuous-flow left ventricular assist device unloading in chronic heart failure: insights into cardiac recovery. J Am Coll Cardiol, 61, 1985–94. [PubMed: 23500219]

DZIMIRI N 1999. Regulation of beta-adrenoceptor signaling in cardiac function and disease. Pharmacol Rev, 51, 465–501. [PubMed: 10471415]

EWELS P, MAGNUSSON M, LUNDIN S & KALLER M 2016. MultiQC: summarize analysis results for multiple tools and samples in a single report. Bioinformatics, 32, 3047–8. [PubMed: 27312411]

FILLMORE N, LEVASSEUR JL, FUKUSHIMA A, WAGG CS, WANG W, DYCK JRB & LOPASCHUK GD 2018. Uncoupling of glycolysis from glucose oxidation accompanies the development of heart failure with preserved ejection fraction. Mol Med, 24, 3. [PubMed: 30134787]

FLORES A, SCHELL J, KRALL AS, JELINEK D, MIRANDA M, GRIGORIAN M, BRAAS D, WHITE AC, ZHOU JL, GRAHAM NA, GRAEBER T, SETH P, EVSEENKO D, COLLER HA, RUTTER J, CHRISTOFK HR & LOWRY WE 2017. Lactate dehydrogenase activity drives hair follicle stem cell activation. Nat Cell Biol, 19, 1017–1026. [PubMed: 28812580]

GABRIEL-COSTA D, CUNHA TF, PAIXAO NA, FORTUNATO RS, REGO-MONTEIRO ICC, BARRETO-CHAVES MLM & BRUM PC 2018. Lactate-upregulation of lactate oxidation complex-related genes is blunted in left ventricle of myocardial infarcted rats. Braz J Med Biol Res, 51, e7660. [PubMed: 30304133]

GABRIEL-COSTA D, DA CUNHA TF, BECHARA LR, FORTUNATO RS, BOZI LH, COELHO MDE A, BARRETO-CHAVES ML & BRUM PC 2015. Lactate up-regulates the expression of lactate oxidation complex-related genes in left ventricular cardiac tissue of rats. PLoS One, 10, e0127843. [PubMed: 25996919]

GERTZ EW, WISNESKI JA, STANLEY WC & NEESE RA 1988. Myocardial substrate utilization during exercise in humans. Dual carbon-labeled carbohydrate isotope experiments. J Clin Invest, 82, 2017–25. [PubMed: 3198763]

GOPAL K, ALMUTAIRI M, AL BATRAN R, EATON F, GANDHI M & USSHER JR 2018. Cardiac-Specific Deletion of Pyruvate Dehydrogenase Impairs Glucose Oxidation Rates and Induces Diastolic Dysfunction. Front Cardiovasc Med, 5, 17. [PubMed: 29560354]

GRAY LR, SULTANA MR, RAUCKHORST AJ, OONTHONPAN L, TOMPKINS SC, SHARMA A, FU X, MIAO R, PEWA AD, BROWN KS, LANE EE, DOHLMAN A, ZEPEDA-OROZCO D, XIE J, RUTTER J, NORRIS AW, COX JE, BURGESS SC, POTTHOFF MJ & TAYLOR EB 2015. Hepatic Mitochondrial Pyruvate Carrier 1 Is Required for Efficient Regulation of Gluconeogenesis and Whole-Body Glucose Homeostasis. Cell Metab, 22, 669–81. [PubMed: 26344103]

GRENELL A, WANG Y, YAM M, SWARUP A, DILAN TL, HAUER A, LINTON JD, PHILP NJ, GREGOR E, ZHU S, SHI Q, MURPHY J, GUAN T, LOHNER D, KOLANDAIVELU S, RAMAMURTHY V, GOLDBERG AFX, HURLEY JB & DU J 2019. Loss of MPC1 reprograms retinal metabolism to impair visual function. Proc Natl Acad Sci U S A, 116, 3530–3535. [PubMed: 30808746]

GROUSSARD C, MOREL I, CHEVANNE M, MONNIER M, CILLARD J & DELAMARCHE A 2000. Free radical scavenging and antioxidant effects of lactate ion: an in vitro study. J Appl Physiol (1985), 89, 169–75. [PubMed: 10904049]

GUI DY, SULLIVAN LB, LUENGO A, HOSIOS AM, BUSH LN, GITEGO N, DAVIDSON SM, FREINKMAN E, THOMAS CJ & VANDER HEIDEN MG 2016. Environment Dictates Dependence on Mitochondrial Complex I for NAD+ and Aspartate Production and Determines Cancer Cell Sensitivity to Metformin. Cell Metab, 24, 716–727. [PubMed: 27746050]

HARBAUER AB, ZAHEDI RP, SICKMANN A, PFANNER N & MEISINGER C 2014. The protein import machinery of mitochondria-a regulatory hub in metabolism, stress, and disease. Cell Metab, 19, 357–72. [PubMed: 24561263]

HARRIS CR, MILLMAN KJ, VAN DER WALT SJ, GOMMERS R, VIRTANEN P, COURNAPEAU D, WIESER E, TAYLOR J, BERG S, SMITH NJ, KERN R, PICUS M, HOYER S, VAN KERKWIJK MH, BRETT M, HALDANE A, DEL RIO JF, WIEBE M, PETERSON P, GERARD-MARCHANT P, SHEPPARD K, REDDY T, WECKESSER W, ABBASI H, GOHLKE C & OLIPHANT TE 2020. Array programming with NumPy. Nature, 585, 357–362. [PubMed: 32939066]

HERZ H, BLAKE DR & GROOTVELD M 1997. Multicomponent investigations of the hydrogen peroxide- and hydroxyl radical-scavenging antioxidant capacities of biofluids: the roles of endogenous pyruvate and lactate. Relevance to inflammatory joint diseases. Free Radic Res, 26, 19–35. [PubMed: 9018469]

HUI S, GHERGUROVICH JM, MORSCHER RJ, JANG C, TENG X, LU W, ESPARZA LA, REYA T, LE Z, YANXIANG GUO J, WHITE E & RABINOWITZ JD 2017. Glucose feeds the TCA cycle via circulating lactate. Nature, 551, 115–118. [PubMed: 29045397]

HUNTER JD 2007. Matplotlib: A 2D Graphics Environment. Computing in Science & Engineering, 9, 90–95.

ITO H, HIRATA Y, ADACHI S, TANAKA M, TSUJINO M, KOIKE A, NOGAMI A, MURUMO F & HIROE M 1993. Endothelin-1 is an autocrine/paracrine factor in the mechanism of angiotensin II-induced hypertrophy in cultured rat cardiomyocytes. J Clin Invest, 92, 398–403. [PubMed: 8326007]

JESSUP M & BROZENA S 2003. Heart failure. N Engl J Med, 348, 2007–18. [PubMed: 12748317]

KARWI QG, UDDIN GM, HO KL & LOPASCHUK GD 2018. Loss of Metabolic Flexibility in the Failing Heart. Front Cardiovasc Med, 5, 68. [PubMed: 29928647]

KASPER EK, AGEMA WR, HUTCHINS GM, DECKERS JW, HARE JM & BAUGHMAN KL 1994. The causes of dilated cardiomyopathy: a clinicopathologic review of 673 consecutive patients. J Am Coll Cardiol, 23, 586–90. [PubMed: 8113538]

KHATTAR RS, SENIOR R, SOMAN P, VAN DER DOES R & LAHIRI A 2001. Regression of left ventricular remodeling in chronic heart failure: Comparative and combined effects of captopril and carvedilol. Am Heart J, 142, 704–13. [PubMed: 11579363]

KIRK P, WILSON MC, HEDDLE C, BROWN MH, BARCLAY AN & HALESTRAP AP 2000. CD147 is tightly associated with lactate transporters MCT1 and MCT4 and facilitates their cell surface expression. EMBO J, 19, 3896–904. [PubMed: 10921872]

KOLWICZ SC JR., PUROHIT S & TIAN R 2013. Cardiac metabolism and its interactions with contraction, growth, and survival of cardiomyocytes. Circ Res, 113, 603–16. [PubMed: 23948585]

LESNEFSKY EJ, MOGHADDAS S, TANDLER B, KERNER J & HOPPEL CL 2001. Mitochondrial dysfunction in cardiac disease: ischemia--reperfusion, aging, and heart failure. J Mol Cell Cardiol, 33, 1065–89. [PubMed: 11444914]

LIAO Y, SMYTH GK & SHI W 2014. featureCounts: an efficient general purpose program for assigning sequence reads to genomic features. Bioinformatics, 30, 923–30. [PubMed: 24227677]

LIM KS, LIM KJ, PRICE AC, ORR BA, EBERHART CG & BAR EE 2014. Inhibition of monocarboxylate transporter-4 depletes stem-like glioblastoma cells and inhibits HIF transcriptional response in a lactate-independent manner. Oncogene, 33, 4433–41. [PubMed: 24077291]

LIU X, COOPER DE, CLUNTUN AA, WARMOES MO, ZHAO S, REID MA, LIU J, LUND PJ, LOPES M, GARCIA BA, WELLEN KE, KIRSCH DG & LOCASALE JW 2018. Acetate Production from Glucose and Coupling to Mitochondrial Metabolism in Mammals. Cell, 175, 502–513 e13. [PubMed: 30245009]

LOVE MI, HUBER W & ANDERS S 2014. Moderated estimation of fold change and dispersion for RNA-seq data with DESeq2. Genome Biol, 15, 550. [PubMed: 25516281]

LU G, JIA Z, ZU Q, ZHANG J, ZHAO L & SHI H 2018. Inhibition of the cyclophilin A-CD147 interaction attenuates right ventricular injury and dysfunction after acute pulmonary embolism in rats. J Biol Chem, 293, 12199–12208. [PubMed: 29914983]

LUKEY MJ, CLUNTUN AA, KATT WP, LIN MJ, DRUSO JE, RAMACHANDRAN S, ERICKSON JW, LE HH, WANG ZE, BLANK B, GREENE KS & CERIONE RA 2019. Liver-Type Glutaminase GLS2 Is a Druggable Metabolic Node in Luminal-Subtype Breast Cancer. Cell Rep, 29, 76–88 e7. [PubMed: 31577957]

MARCHIQ I, LE FLOCH R, ROUX D, SIMON MP & POUYSSEGUR J 2015. Genetic disruption of lactate/H+ symporters (MCTs) and their subunit CD147/BASIGIN sensitizes glycolytic tumor cells to phenformin. Cancer Res, 75, 171–80. [PubMed: 25403912]

MARTIN M 2011. Cutadapt removes adapter sequences from high-throughput sequencing reads. 2011, 17, 3.

MCCLELLAND GB & BROOKS GA 2002. Changes in MCT 1, MCT 4, and LDH expression are tissue specific in rats after long-term hypobaric hypoxia. J Appl Physiol (1985), 92, 1573–84. [PubMed: 11896024]

MCCOMMIS KS, CHEN Z, FU X, MCDONALD WG, COLCA JR, KLETZIEN RF, BURGESS SC & FINCK BN 2015. Loss of Mitochondrial Pyruvate Carrier 2 in the Liver Leads to Defects in Gluconeogenesis and Compensation via Pyruvate-Alanine Cycling. Cell Metab, 22, 682–94. [PubMed: 26344101]

MCNALLY EM & MESTRONI L 2017. Dilated Cardiomyopathy: Genetic Determinants and Mechanisms. Circ Res, 121, 731–748. [PubMed: 28912180]

METRA M & TEERLINK JR 2017. Heart failure. Lancet, 390, 1981–1995. [PubMed: 28460827]

MURRAY CM, HUTCHINSON R, BANTICK JR, BELFIELD GP, BENJAMIN AD, BRAZMA D, BUNDICK RV, COOK ID, CRAGGS RI, EDWARDS S, EVANS LR, HARRISON R, HOLNESS E, JACKSON AP, JACKSON CG, KINGSTON LP, PERRY MW, ROSS AR, RUGMAN PA, SIDHU SS, SULLIVAN M, TAYLOR-FISHWICK DA, WALKER PC, WHITEHEAD YM, WILKINSON DJ, WRIGHT A & DONALD DK 2005. Monocarboxylate transporter MCT1 is a target for immunosuppression. Nat Chem Biol, 1, 371–6. [PubMed: 16370372]

OPIE L 1980. Lactate metabolism and cardiac muscle. Lactate. Springer.

PALMIERI F 2013. The mitochondrial transporter family SLC25: identification, properties and physiopathology. Mol Aspects Med, 34, 465–84. [PubMed: 23266187]

PEDREGOSA F, VAROQUAUX G, GRAMFORT A, MICHEL V, THIRION B, GRISEL O, BLONDEL M, PRETTENHOFER P, WEISS R, DUBOURG V, VANDERPLAS J, PASSOS A, COURNAPEAU D, BRUCHER M, PERROT M & DUCHESNAY É 2011. Scikit-learn: Machine Learning in Python. J. Mach. Learn. Res, 12, 2825–2830.

PICARD M, MCMANUS MJ, CSORDAS G, VARNAI P, DORN GW 2ND, WILLIAMS D, HAJNOCZKY G & WALLACE DC 2015. Trans-mitochondrial coordination of cristae at regulated membrane junctions. Nat Commun, 6, 6259. [PubMed: 25687472]

PRICE NT, JACKSON VN & HALESTRAP AP 1998. Cloning and sequencing of four new mammalian monocarboxylate transporter (MCT) homologues confirms the existence of a transporter family with an ancient past. Biochem J, 329 (Pt 2), 321–8. [PubMed: 9425115]

RAUCKHORST AJ, GRAY LR, SHELDON RD, FU X, PEWA AD, FEDDERSEN CR, DUPUY AJ, GIBSON-CORLEY KN, COX JE, BURGESS SC & TAYLOR EB 2017. The mitochondrial pyruvate carrier mediates high fat diet-induced increases in hepatic TCA cycle capacity. Mol Metab, 6, 1468–1479. [PubMed: 29107293]

REIMAND J, KULL M, PETERSON H, HANSEN J & VILO J 2007. g:Profiler--a web-based toolset for functional profiling of gene lists from large-scale experiments. Nucleic Acids Res, 35, W193–200. [PubMed: 17478515]

RITTERHOFF J & TIAN R 2017. Metabolism in cardiomyopathy: every substrate matters. Cardiovasc Res, 113, 411–421. [PubMed: 28395011]

RITTERHOFF J, YOUNG S, VILLET O, SHAO D, NETO FC, BETTCHER LF, HSU YA, KOLWICZ SC, RAFTERY D & TIAN R 2019. Metabolic Remodeling Promotes Cardiac Hypertrophy by Directing Glucose to Aspartate Biosynthesis. Circ Res.

SAFER B 1975. The Metabolic Significance of the Malate-Aspartate Cycle in Heart. Circ Res, 37, 527–33. [PubMed: 172258]

SAVARESE G & LUND LH 2017. Global Public Health Burden of Heart Failure. Card Fail Rev, 3, 7–11. [PubMed: 28785469]

SCHELL JC, WISIDAGAMA DR, BENSARD C, ZHAO H, WEI P, TANNER J, FLORES A, MOHLMAN J, SORENSEN LK, EARL CS, OLSON KA, MIAO R, WALLER TC, DELKER D, KANTH P, JIANG L, DEBERARDINIS RJ, BRONNER MP, LI DY, COX JE, CHRISTOFK HR, LOWRY WE, THUMMEL CS & RUTTER J 2017. Control of intestinal stem cell function and proliferation by mitochondrial pyruvate metabolism. Nat Cell Biol, 19, 1027–1036. [PubMed: 28812582]

SEYMOUR AM & CHATHAM JC 1997. The effects of hypertrophy and diabetes on cardiac pyruvate dehydrogenase activity. J Mol Cell Cardiol, 29, 2771–8. [PubMed: 9344771]

SHAO D, VILLET O, ZHANG Z, CHOI SW, YAN J, RITTERHOFF J, GU H, DJUKOVIC D, CHRISTODOULOU D, KOLWICZ SC JR., RAFTERY D & TIAN R 2018. Glucose promotes cell growth by suppressing branched-chain amino acid degradation. Nat Commun, 9, 2935. [PubMed: 30050148]

SHARMA A, OONTHONPAN L, SHELDON RD, RAUCKHORST AJ, ZHU Z, TOMPKINS SC, CHO K, GRZESIK WJ, GRAY LR, SCERBO DA, PEWA AD, CUSHING EM, DYLE MC, COX JE, ADAMS C, DAVIES BS, SHIELDS RK, NORRIS AW, PATTI G, ZINGMAN LV & TAYLOR EB 2019. Impaired skeletal muscle mitochondrial pyruvate uptake rewires glucose metabolism to drive whole-body leanness. Elife, 8.

SHEERAN FL, ANGEROSA J, LIAW NY, CHEUNG MM & PEPE S 2019. Adaptations in Protein Expression and Regulated Activity of Pyruvate Dehydrogenase Multienzyme Complex in Human Systolic Heart Failure. Oxid Med Cell Longev, 2019, 4532592. [PubMed: 30881593]

SOHAL DS, NGHIEM M, CRACKOWER MA, WITT SA, KIMBALL TR, TYMITZ KM, PENNINGER JM & MOLKENTIN JD 2001. Temporally regulated and tissue-specific gene manipulations in the adult and embryonic heart using a tamoxifen-inducible Cre protein. Circ Res, 89, 20–5. [PubMed: 11440973]

SPRIET LL, HOWLETT RA & HEIGENHAUSER GJ 2000. An enzymatic approach to lactate production in human skeletal muscle during exercise. Med Sci Sports Exerc, 32, 756–63. [PubMed: 10776894]

SUGDEN MC & HOLNESS MJ 2003. Recent advances in mechanisms regulating glucose oxidation at the level of the pyruvate dehydrogenase complex by PDKs. Am J Physiol Endocrinol Metab, 284, E855–62. [PubMed: 12676647]

SULLIVAN LB, GUI DY, HOSIOS AM, BUSH LN, FREINKMAN E & VANDER HEIDEN MG 2015. Supporting Aspartate Biosynthesis Is an Essential Function of Respiration in Proliferating Cells. Cell, 162, 552–63. [PubMed: 26232225]

SUZUKI K, SATOH K, IKEDA S, SUNAMURA S, OTSUKI T, SATOH T, KIKUCHI N, OMURA J, KUROSAWA R, NOGI M, NUMANO K, SUGIMURA K, AOKI T, TATEBE S, MIYATA S, MUKHERJEE R, SPINALE FG, KADOMATSU K & SHIMOKAWA H 2016. Basigin Promotes Cardiac Fibrosis and Failure in Response to Chronic Pressure Overload in Mice. Arterioscler Thromb Vasc Biol, 36, 636–46. [PubMed: 26916734]

THAM YK, BERNARDO BC, OOI JY, WEEKS KL & MCMULLEN JR 2015. Pathophysiology of cardiac hypertrophy and heart failure: signaling pathways and novel therapeutic targets. Arch Toxicol, 89, 1401–38. [PubMed: 25708889]

TODENHOFER T, SEILER R, STEWART C, MOSKALEV I, GAO J, LADHAR S, KAMJABI A, AL NAKOUZI N, HAYASHI T, CHOI S, WANG Y, FREES S, DAUGAARD M, OO HZ, FISEL P, SCHWAB M, SCHAEFFELER E, DOUGLAS J, HENNENLOTTER J, BEDKE J, GIBB EA, FAZLI L, STENZL A & BLACK PC 2018. Selective Inhibition of the Lactate Transporter MCT4 Reduces Growth of Invasive Bladder Cancer. Mol Cancer Ther, 17, 2746–2755. [PubMed: 30262589]

TOPKARA VK, GARAN AR, FINE B, GODIER-FURNEMONT AF, BRESKIN A, CAGLIOSTRO B, YUZEFPOLSKAYA M, TAKEDA K, TAKAYAMA H, MANCINI DM, NAKA Y & COLOMBO PC 2016. Myocardial Recovery in Patients Receiving Contemporary Left Ventricular Assist Devices: Results From the Interagency Registry for Mechanically Assisted Circulatory Support (INTERMACS). Circ Heart Fail, 9.

TRAN DH & WANG ZV 2019. Glucose Metabolism in Cardiac Hypertrophy and Heart Failure. J Am Heart Assoc, 8, e012673. [PubMed: 31185774]

UHLEN M, FAGERBERG L, HALLSTROM BM, LINDSKOG C, OKSVOLD P, MARDINOGLU A, SIVERTSSON A, KAMPF C, SJOSTEDT E, ASPLUND A, OLSSON I, EDLUND K, LUNDBERG E, NAVANI S, SZIGYARTO CA, ODEBERG J, DJUREINOVIC D, TAKANEN JO, HOBER S, ALM T, EDQVIST PH, BERLING H, TEGEL H, MULDER J, ROCKBERG J, NILSSON P, SCHWENK JM, HAMSTEN M, VON FEILITZEN K, FORSBERG M, PERSSON L, JOHANSSON F, ZWAHLEN M, VON HEIJNE G, NIELSEN J & PONTEN F 2015. Proteomics. Tissue-based map of the human proteome. Science, 347, 1260419. [PubMed: 25613900]

UMBARAWAN Y, SYAMSUNARNO M, KOITABASHI N, YAMAGUCHI A, HANAOKA H, HISHIKI T, NAGAHATA-NAITO Y, OBINATA H, SANO M, SUNAGA H, MATSUI H, TSUSHIMA Y, SUEMATSU M, KURABAYASHI M & ISO T 2018. Glucose is preferentially utilized for biomass synthesis in pressure-overloaded hearts: evidence from fatty acid-binding protein-4 and −5 knockout mice. Cardiovasc Res, 114, 1132–1144. [PubMed: 29554241]

WAI T, GARCIA-PRIETO J, BAKER MJ, MERKWIRTH C, BENIT P, RUSTIN P, RUPEREZ FJ, BARBAS C, IBANEZ B & LANGER T 2015. Imbalanced OPA1 processing and mitochondrial fragmentation cause heart failure in mice. Science, 350, aad0116.

WATKINS SJ, BORTHWICK GM & ARTHUR HM 2011. The H9C2 cell line and primary neonatal cardiomyocyte cells show similar hypertrophic responses in vitro. In Vitro Cell Dev Biol Anim, 47, 125–31. [PubMed: 21082279]

WEIBEL ER, KISTLER GS & SCHERLE WF 1966. Practical stereological methods for morphometric cytology. J Cell Biol, 30, 23–38. [PubMed: 5338131]

WEVER-PINZON J, SELZMAN CH, STODDARD G, WEVER-PINZON O, CATINO A, KFOURY AG, DIAKOS NA, REID BB, MCKELLAR S, BONIOS M, KOLIOPOULOU A, BUDGE D, KELKHOFF A, STEHLIK J, FANG JC & DRAKOS SG 2016a. Impact of Ischemic Heart Failure Etiology on Cardiac Recovery During Mechanical Unloading. J Am Coll Cardiol, 68, 1741–1752. [PubMed: 27737740]

WEVER-PINZON O, DRAKOS SG, MCKELLAR SH, HORNE BD, CAINE WT, KFOURY AG, LI DY, FANG JC, STEHLIK J & SELZMAN CH 2016b. Cardiac Recovery During Long-Term Left Ventricular Assist Device Support. J Am Coll Cardiol, 68, 1540–53. [PubMed: 27687196]

WILSON MC, JACKSON VN, HEDDLE C, PRICE NT, PILEGAARD H, JUEL C, BONEN A, MONTGOMERY I, HUTTER OF & HALESTRAP AP 1998. Lactic acid efflux from white skeletal muscle is catalyzed by the monocarboxylate transporter isoform MCT3. J Biol Chem, 273, 15920–6. [PubMed: 9632638]

WISNESKI JA, GERTZ EW, NEESE RA, GRUENKE LD, MORRIS DL & CRAIG JC 1985. Metabolic fate of extracted glucose in normal human myocardium. J Clin Invest, 76, 1819–27. [PubMed: 4056055]

XIA J & WISHART DS 2011. Web-based inference of biological patterns, functions and pathways from metabolomic data using MetaboAnalyst. Nat Protoc, 6, 743–60. [PubMed: 21637195]

YANAGIDA S, LUO CS, DOYLE M, POHOST GM & PIKE MM 1995. Nuclear magnetic resonance studies of cationic and energetic alterations with oxidant stress in the perfused heart. Modulation with pyruvate and lactate. Circ Res, 77, 773–83. [PubMed: 7554125]

YANCY CW, JESSUP M, BOZKURT B, BUTLER J, CASEY DE JR., COLVIN MM, DRAZNER MH, FILIPPATOS GS, FONAROW GC, GIVERTZ MM, HOLLENBERG SM, LINDENFELD J, MASOUDI FA, MCBRIDE PE, PETERSON PN, STEVENSON LW & WESTLAKE C 2017. 2017 ACC/AHA/HFSA Focused Update of the 2013 ACCF/AHA Guideline for the Management of Heart Failure: A Report of the American College of Cardiology/American Heart Association Task Force on Clinical Practice Guidelines and the Heart Failure Society of America. Circulation, 136, e137–e161. [PubMed: 28455343]

ZHOU B & TIAN R 2018. Mitochondrial dysfunction in pathophysiology of heart failure. J Clin Invest, 128, 3716–3726. [PubMed: 30124471]

ZHU Y, WU J & YUAN SY 2013. MCT1 and MCT4 expression during myocardial ischemic-reperfusion injury in the isolated rat heart. Cell Physiol Biochem, 32, 663–74. [PubMed: 24030048]

ZORDOKY BN & EL-KADI AO 2007. H9c2 cell line is a valuable in vitro model to study the drug metabolizing enzymes in the heart. J Pharmacol Toxicol Methods, 56, 317–22. [PubMed: 17662623]

ZOROVA LD, POPKOV VA, PLOTNIKOV EY, SILACHEV DN, PEVZNER IB, JANKAUSKAS SS, BABENKO VA, ZOROV SD, BALAKIREVA AV, JUHASZOVA M, SOLLOTT SJ & ZOROV DB 2018. Mitochondrial membrane potential. Anal Biochem, 552, 50–59. [PubMed: 28711444]

Highlights

- Myocardial MPC expression coincides with LVAD-mediated recovery in chronic HF patients.
- Loss of the MPC in cultured cells and in murine hearts is sufficient to induce hypertrophy and HF.
- MPC overexpression attenuates drug-induced hypertrophy in a cell-autonomous manner.
- Inhibition of MCT4 can mitigate hypertrophy in cultured cardiomyocytes and in mice.

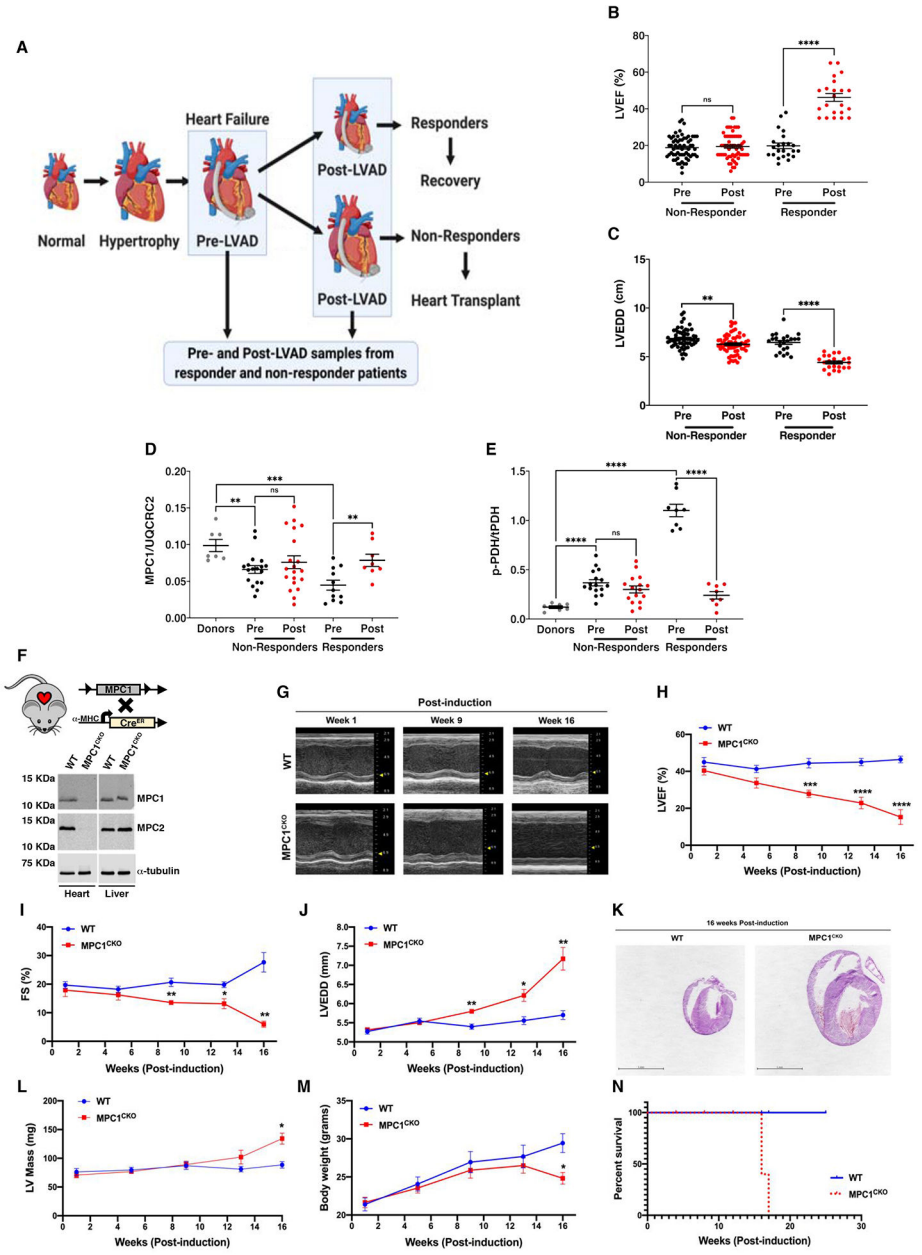

Figure 1. MPC1 deficiency is sufficient to promote cardiac hypertrophy and leads to heart failure

(A) Diagram depicting progression of hearts towards HF and how paired HF patient hearts were compared pre and post LVAD unloading.

(B and C) Scatter dot plots comparing paired left ventricular ejection fractions (LVEF), and left ventricular end diastolic diameters (LVEDD) from human hearts of non-responder (n=60) and responder (n=23) HF patients pre and post LVAD unloading.

(D and E) Western blot densitometric results showing MPC1 and p-PDH/PDH levels in human LV tissues from non-failing donors (n=7), non-responders (Pre, n=18, Post, n=21) and responders (Pre, n=12, Post, n=8) (Pre, Pre-LVAD time point; Post, Post-LVAD time point).

(F) Representative western blot analysis of MPC1 and MPC2 proteins in LV and liver tissue lysates from wild type (WT) and MPC1 cardiac-specific knock out (*MPC1*^{CKO}) mice (n=5). Schematics of the *MPC1*^{flox} and α-*MHC-Cre*^{ER} alleles are shown.
(G) Representative images of M-mode echocardiography recorded from LV of WT and *MPC1*^{CKO} mice after 1, 11- and 16-weeks post-induction, showing hypertrophy and LV dilation (n=7).
(H, I and J) Time course of change in LVEF, Fractional shortening (FS) and LVEDD of WT and *MPC1*^{CKO} mice (n=7).
(K) Representative H&E stained sections of hearts from WT and *MPC1*^{CKO} mice (n=3).
(L) LV mass of WT and *MPC1*^{CKO} mice (n=7).
(M) Weight of WT and *MPC1*^{CKO} mice (n=7).
(N) Kaplan-Meier survival curve of WT and *MPC1*^{CKO} mice. WT n=4 and *MPC1*^{CKO} n=4. Data are presented as mean ± SEM, *p<0.05, **p<0.01**, ***p<0.001, ****p<0.0001, determined by one-way ANOVA and Sidak's multiple comparison test (B–E), student's unpaired t test (H–J, L and M) and Log-rank and Wilcoxon tests (N). ns, not significant. See also Figure S1 and Table 1.

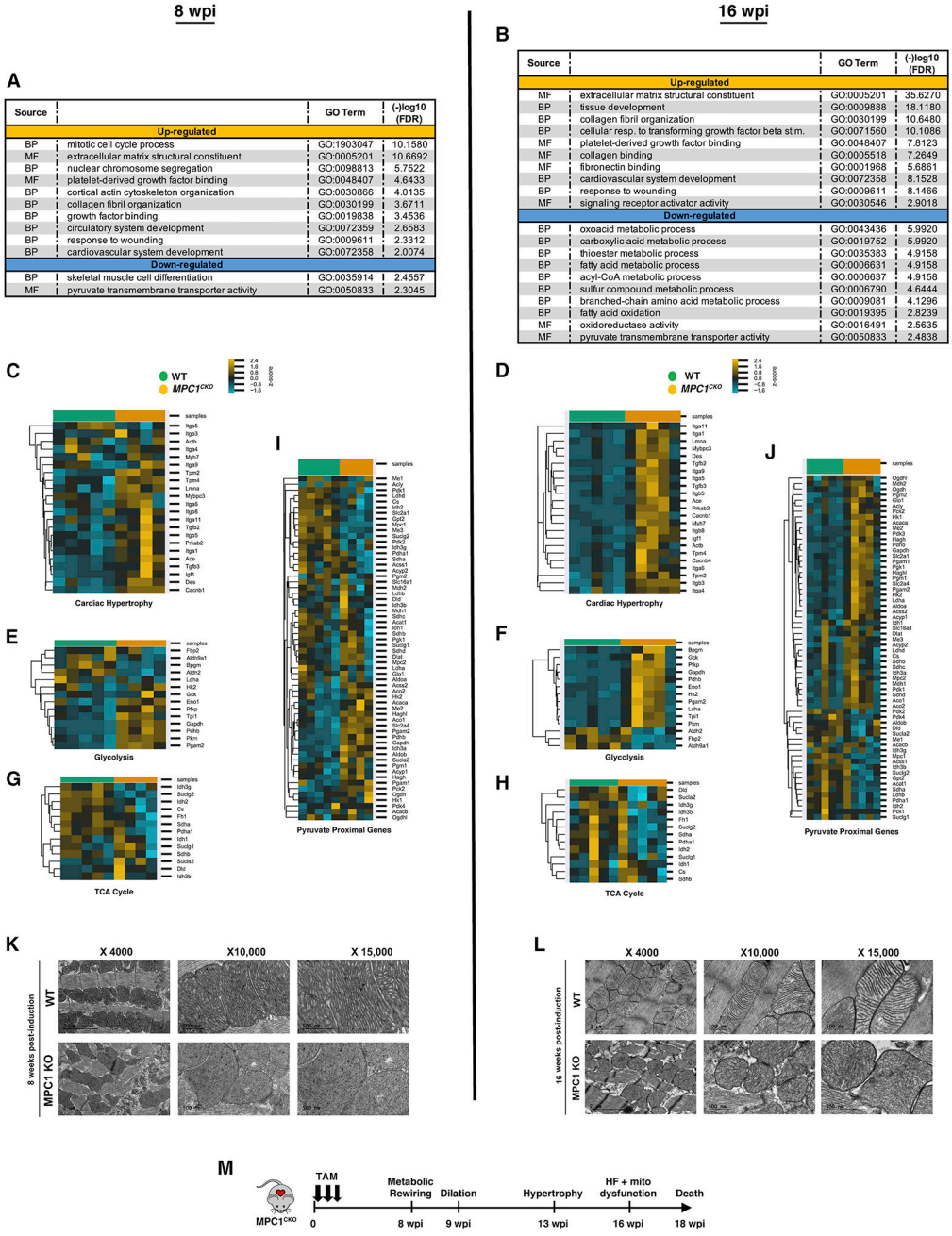

Source		GO Term	(-)log10 (FDR)
Up-regulated			
BP	mitotic cell cycle process	GO:1903047	10.1580
MF	extracellular matrix structural constituent	GO:0005201	10.6692
BP	nuclear chromosome segregation	GO:0098813	5.7522
MF	platelet-derived growth factor binding	GO:0048407	4.6433
BP	cortical actin cytoskeleton organization	GO:0030866	4.0135
BP	collagen fibril organization	GO:0030199	3.6711
BP	growth factor binding	GO:0019838	3.4536
BP	circulatory system development	GO:0072359	2.6583
BP	response to wounding	GO:0009611	2.3312
BP	cardiovascular system development	GO:0072358	2.0074
Down-regulated			
BP	skeletal muscle cell differentiation	GO:0035914	2.4557
MF	pyruvate transmembrane transporter activity	GO:0050833	2.3045

Source		GO Term	(-)log10 (FDR)
Up-regulated			
MF	extracellular matrix structural constituent	GO:0005201	35.6270
BP	tissue development	GO:0009888	18.1180
BP	collagen fibril organization	GO:0030199	10.6480
BP	cellular resp. to transforming growth factor beta stim.	GO:0071560	10.1086
MF	platelet-derived growth factor binding	GO:0048407	7.8123
MF	collagen binding	GO:0005518	7.2649
MF	fibronectin binding	GO:0001968	5.6861
BP	cardiovascular system development	GO:0072358	8.1528
BP	response to wounding	GO:0009611	8.1466
MF	signaling receptor activator activity	GO:0030546	2.9018
Down-regulated			
BP	oxoacid metabolic process	GO:0043436	5.9920
BP	carboxylic acid metabolic process	GO:0019752	5.9920
BP	thioester metabolic process	GO:0035383	4.9158
BP	fatty acid metabolic process	GO:0006631	4.9158
BP	acyl-CoA metabolic process	GO:0006637	4.9158
BP	sulfur compound metabolic process	GO:0006790	4.6444
BP	branched-chain amino acid metabolic process	GO:0009081	4.1296
BP	fatty acid oxidation	GO:0019395	2.8239
MF	oxidoreductase activity	GO:0016491	2.5635
MF	pyruvate transmembrane transporter activity	GO:0050833	2.4838

Figure 2. Loss of MPC is an early injury in HF

(A) GO term analysis on up-regulated genes in *MPC1*^{CKO} mice at 8 weeks post induction (wpi). (MF, molecular function; BP, biological process). Murine heart tissue was harvested from WT mice (green) (n=4) and *MPC1*^{CKO} (orange) (n=4).

(B) GO term analysis on up-regulated genes in *MPC1*^{CKO} mice at 16wpi. (MF, molecular function; BP, biological process; resp., response; stim., stimulus). Murine heart tissue was harvested from WT mice (green) (n=4) and *MPC1*^{CKO} (orange) (n=4).

(C and D) Changes in cardiac hypertrophy gene set at 8- and 16-wpi.

(E and F) Glycolysis gene set at 8- and 16-wpi.

(G and H) Changes in TCA cycle gene set at 8- and 16-wpi

(I and J) Changes in Pyruvate proximal genes (Bensard et al., 2020) at 8- and 16-wpi. Abundance displayed according to the heatmaps shown. Z-scored genes were clustered via calculating the Euclidean distance between centroids.

(K and L) Representative TEM images at various magnifications of mitochondria from murine LV tissue of *MPC1*^{CKO} and WT at 8 wpi and 16 wpi. RNA was extracted at 8- or 16-wpi and evaluated on custom gene sets including gene components.

(M) 8-week-old *MPC1*^{CKO} mice were injected interperitoneally for 3 consecutive days with TAM (40mg/kg/day) and then examined at 8, 9, 13, and 16 wpi. Assignments were based on the hemodynamic data from Figure 1.

See also Figure S2.

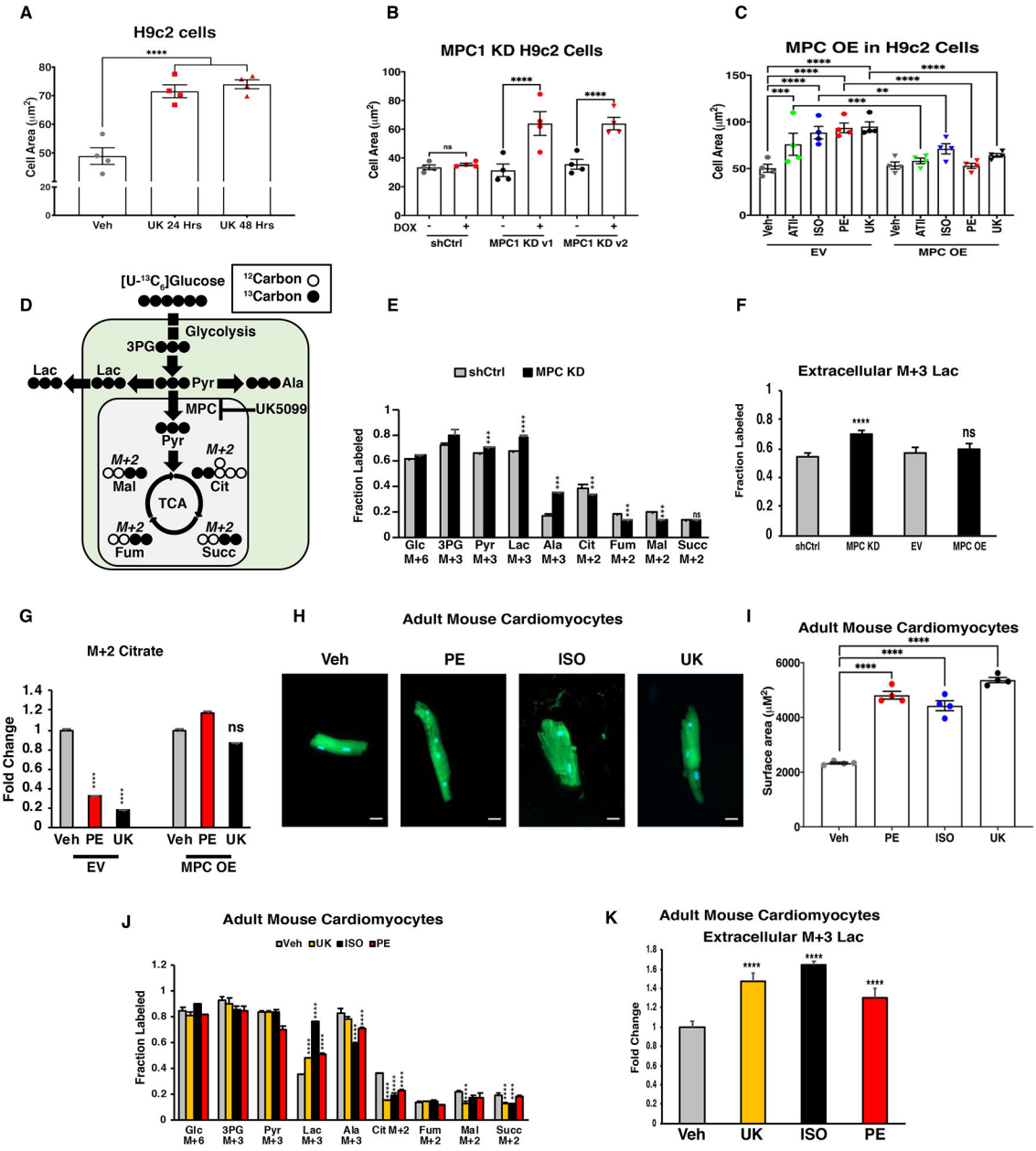

Figure 3. Loss of mitochondrial pyruvate transport is necessary and sufficient to induce hypertrophy in cultured cardiomyocytes

(A) Quantification of cell area of H9c2 cells treated with MPC inhibitor UK5099 (UK).

(B) Quantification of cell area of MPC1 shRNA-mediated knockdown (MPC1 KD) and shRNA control (shCtrl) H9c2 cells.

(C) Quantification of cell area of MPC overexpressing (MPC OE) or control empty vector (EV) H9c2 cells treated with hypertrophic inducing drugs: Angiotensin II (ATII), Isoproterenol (ISO), Phenylephrine (PE) or UK. (n=4, each point is the mean of n≥15 cells from an independent experiment).

(D) Schematic for metabolism of [U-^{13}C]-glucose. White circles depict ^{12}C and black solid circles depict ^{13}C. (3PG, 3-Phosphoglyceric acid; Pyr, Pyruvate; Ala, Alanine; Lac, Lactate; Cit, Citrate; Succ, Succinate; Fum, Fumarate; Mal, Malate).
(E) ^{13}C enrichment of glycolytic and TCA cycle intermediates in MPC1 KD and shCtrl H9c2 cells.
(F) ^{13}C enrichment of extracellular lactate in shCtrl, MPC1 KD, EV and MPC OE H9c2 cells.
(G) Fold change in ^{13}C enrichment of citrate in PE and UK treated EV or MPC OE H9c2 cells relative to Veh.
(H) Representative images of Phalloidin stained primary cultured adult mouse cardiomyocytes that have been treated with DMSO (Veh), UK, PE, or ISO, scale bars, 20μm.
(I) Quantification of cell area of corresponding cardiomyocytes. (n=4, each point is the mean of n≥15 cells from an independent experiment).
(J) ^{13}C enrichment of glycolytic and TCA cycle intermediates in cardiomyocytes.
(K) Fold change in ^{13}C enrichment of extracellular lactate in treated cardiomyocytes relative to the Veh. Data are presented as mean ± SEM, *p<0.05, **p<0.01, ***p<0.001, ****p<0.0001, determined by one-way ANOVA and Sidak's multiple comparison test (A–C, I), and unpaired t test versus Veh (E–G, J, K). ns, not significant.
See also Figure S3.

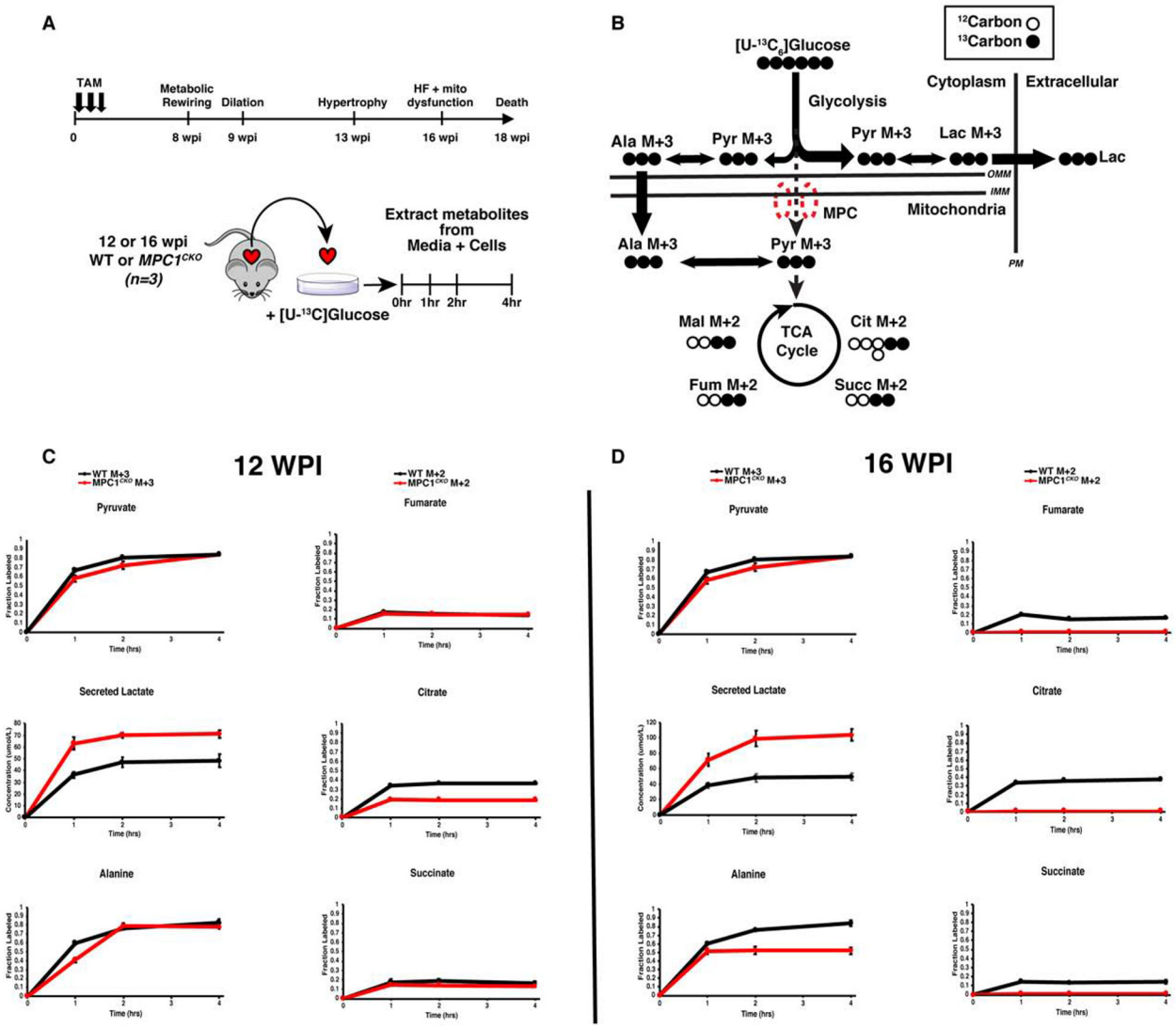

Figure 4. Dynamic changes in glycolytic flux precede hypertrophy and HF in *MPC1*^{CKO} mice

(A) Diagram of experiment, cardiomyocytes were harvested from mice before hypertrophy (12 wpi) and at HF (16 wpi), cultured in media containing [U-^{13}C]-glucose, and metabolites were harvested after 0, 1, 2, and 4 hours.

(B) Schematic of metabolic pathways connecting glycolysis to the TCA cycle. (Pyr, Pyruvate; Lac, Lactate; Ala, Alanine; Cit, Citrate; Succ, Succinate; Fum, Fumarate; Mal, Malate).

(C and D) Dynamic [U^{13}C]-glucose incorporation into corresponding metabolites over time, in primary cultured adult cardiomyocytes harvested from *MPC1*^{CKO} mice at 12 wpi and 16wpi. Data are presented as mean ± SEM.

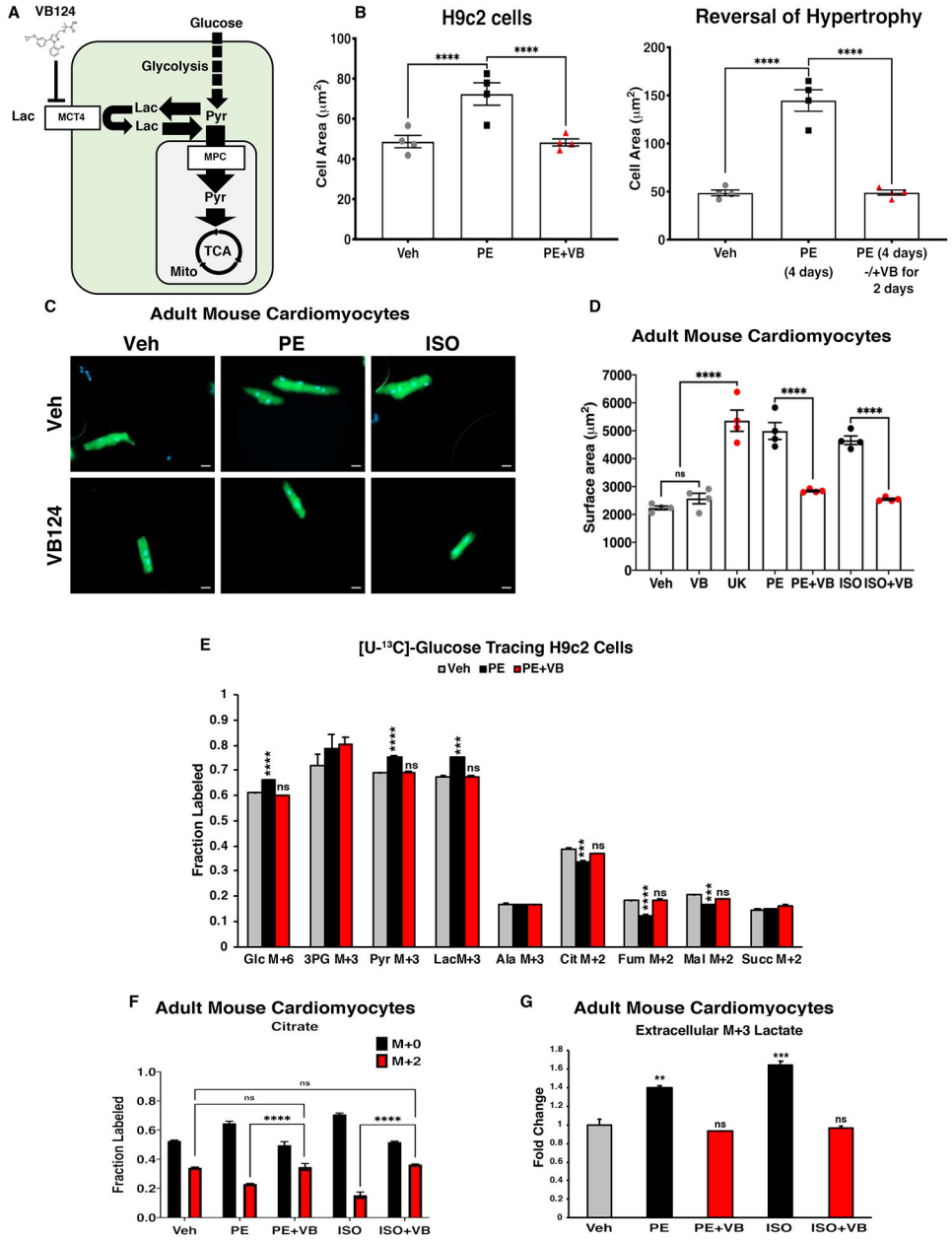

Figure 5. MCT4 inhibition can prevent and reverse hypertrophy in cardiomyocytes

(A) Schematic depicting rewiring of glycolytic flux in hypertrophied cardiomyocytes treated with the MCT4 inhibitor (VB124).

(B) Left: Quantification of cell area of H9c2 cells treated with Veh, PE, PE+VB124 simultaneously or Right: treated with PE and subsequently treated with PE+VB. (n=4, each point is the mean of n≥15 cells from an independent experiment)

(C) Representative images of Phalloidin stained primary cultured adult mouse cardiomyocytes with corresponding treatments: Veh, PE or ISO each with or without VB124. Scale bars, 20μm.

(D) Quantification of surface area of corresponding treated cardiomyocytes, (VB, VB124). (n=4, each point is the mean of n≥15 cells from an independent experiment)

(E) ^{13}C enrichment of glycolytic and TCA cycle intermediates in H9c2 cells treated with Veh, PE, PE+VB, ISO or ISO+VB.

(F) ^{13}C enrichment of Citrate in adult mouse cardiomyocytes.

(G) Fold change in 13C enrichment of extracellular Lactate for adult mouse cardiomyocytes treated with PE, PE+VB, ISO or ISO+VB relative to the Veh. Data are presented as mean ± SEM, *p<0.05, **p<0.01**, ***p<0.001, ****p<0.0001, determined by one-way ANOVA and Sidak's multiple comparison test (B, D) or unpaired t test versus Veh (E–G). ns, not significant.

See also Figure S5.

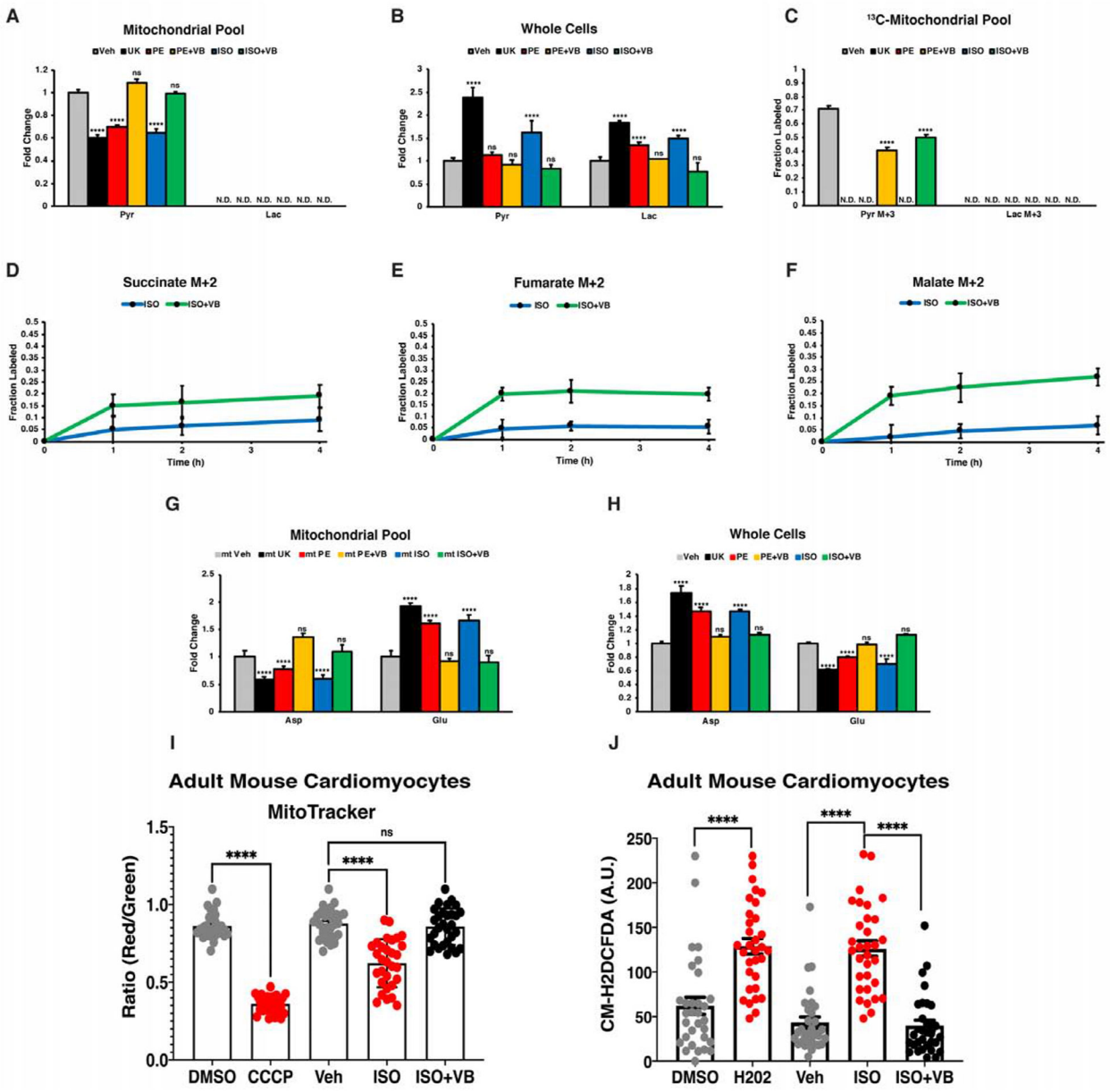

Figure 6. MCT4 inhibition replenishes mitochondrial pyruvate flux, improves mitochondrial membrane potential and mitigates cytosolic ROS

(A) Fold change in mitochondrial matrix specific steady-state unlabeled ^{12}C abundances of Lactate (Lac) and Pyruvate (Pyr) relative to Veh in H9c2 cells treated with UK, PE, PE+VB, ISO and ISO+VB. (N.D., not detected).

(B) Fold change in corresponding whole cell unlabeled ^{12}C abundances of Lac and Pyr relative to the Veh.

(C) ^{13}C enrichment of Lac and Pyr in the mitochondrial matrix specific pool. (N.D., not detected).

(D, E and F) Dynamic ^{13}C-glucose labeling of the TCA cycle intermediates Succinate, Fumarate, and Malate in the mitochondrial matrix over time treated with ISO or ISO+VB.

(G) Fold change in mitochondrial matrix specific steady-state unlabeled ^{12}C abundances of Aspartate (Asp) and Glutamate (Glu) relative to Veh in H9c2 cells treated with UK, PE, PE +VB, ISO and ISO+VB.

(H) Fold change in corresponding whole cell unlabeled ^{12}C abundances of Asp and Glu relative to the Veh.

(I) Ratio of Mitotracker Red and Mitotracker Green in cultured adult mouse cardiomyocytes treated with DMSO, CCCP, Veh, ISO or ISO+VB.

(J) CM-H2DCFDA fluorescence quantification of cultured adult mouse cardiomyocytes treated with DMSO, H_2O_2, Veh, ISO or ISO+VB. Data are presented as mean ± SEM, *p<0.05, **p<0.01**, ***p<0.001, ****p<0.0001, determined by one-way ANOVA and Sidak's multiple comparison test (H, I) or unpaired t test versus Veh (A–C, F, G). ns, not significant.

See also Figure S6.

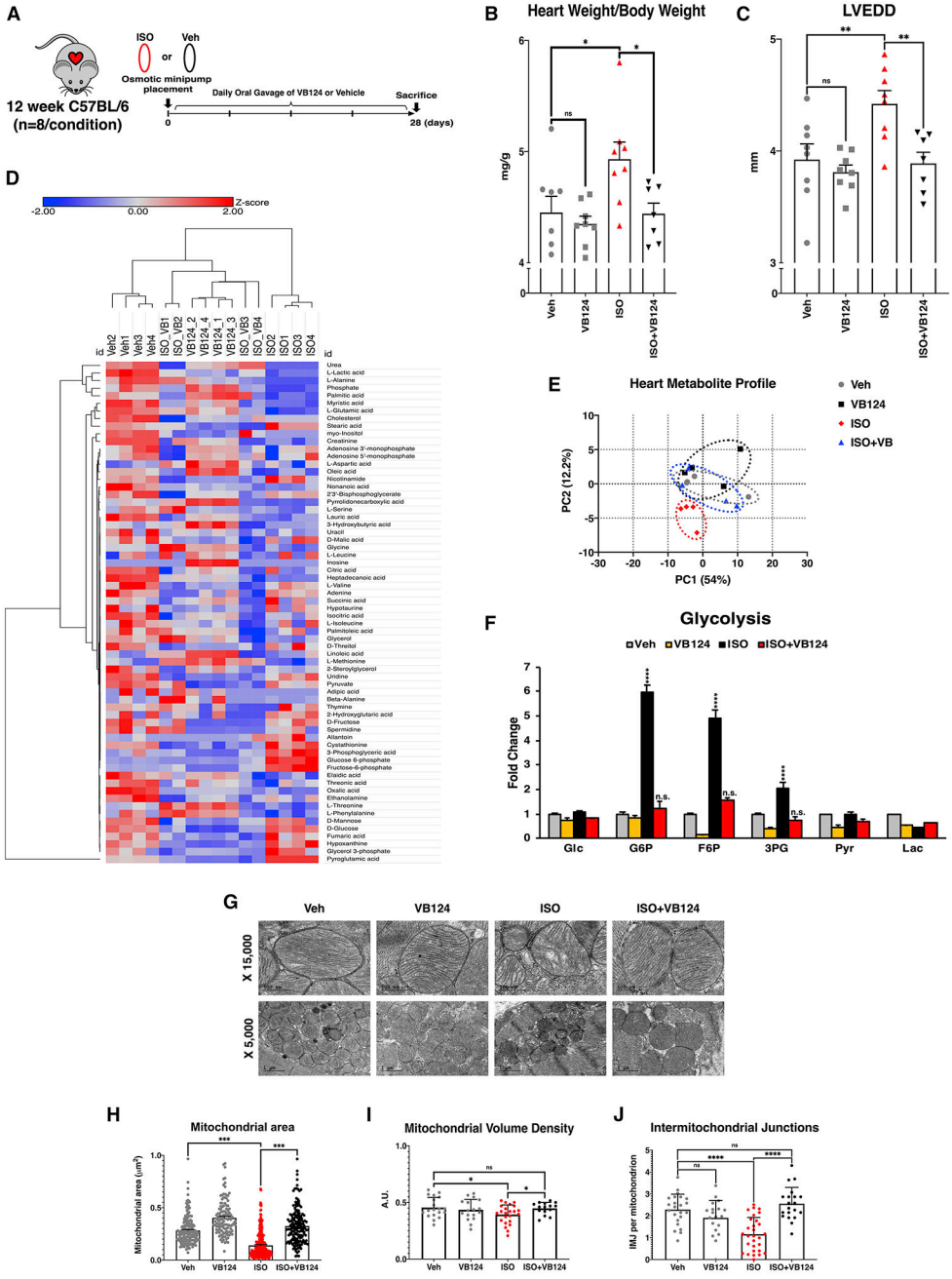

Figure 7. MCT4 inhibition prevents cardiac hypertrophy in mice

(A) Diagram of the experiment, C57BL/6 mice were surgically implanted with osmotic pumps containing ISO or Veh, and were orally gavaged with VB124 or Veh daily for 28 days. (n=8 per condition).

(B) Heart weight to body weight ratio of treated mice.

(C) LV end diastolic diameter (LVEDD) of murine hearts treated with Veh (n=8), VB124 (n=8), ISO (n=8), or ISO+VB124 (n=7) measured from echocardiography.

(D) Clustered heatmap of relative heart metabolite levels (n=4). Metabolites were log2, quantile normalized before Pearson hierarchal clustering, Z-scores calculated by row.

(E) Principle component analysis scores plot of metabolite profiles of corresponding murine hearts.
(F) Fold change in steady-state levels of glycolytic intermediates in VB124, ISO or ISO +MCT4 treated mice relative to the Veh.
(G) Representative heart TEM images of mitochondria from mice following Veh, VB124, ISO or ISO+VB124 treatments at x5,000 and x15,000 magnification.
(H, I and J) Quantification of mitochondrial area, mitochondrial volume density, and intermitochondrial junctions. Data are presented as mean ± SEM, *p<0.05, **p<0.01**,** ***p<0.001, ****p<0.0001, determined by 1-way ANOVA followed by Sidak's multiple comparison (B, C, H–J) or unpaired t test versus Veh (F). ns, not significant.
See also Figure S7.

Table 1.

Clinical characteristics of the chronic heart failure patient population.

Variable	Responders n=12, (mean ± SE)	Non-responders n=21, (mean ± SE)	*p*-value
Male sex, n (%)	10 (83)	15 (71.4)	
Age at LVAD implantation, years	50±5.4	54±3.1	0.74
Pre-LVAD			
LVEDD, cm	6±0.3	6±0.2	0.28
LVEF, %	20±0.3	19±1.6	0.18
Post-LVAD			
LVEDD, cm	5±0.3	6±0.2	<0.001
LVEF, %	48±3	24±1.7	<0.001
HF Etiology			
Ischemic cardiomyopathy, n (%)	4 (33.3)	12 (57.1)	
Non-ischemic cardiomyopathy, n (%)	8 (66.7)	9 (42.9)	
New York Heart Association Functional Class			
III, n (%)	5 (46.7)	6 (28.6)	
IV, n (%)	7 (53.3)	15 (71.4)	
Duration of HF symptoms, months	40±17.3	74±10.1	0.08
Systolic Blood Pressure, mmHg	100±2.8	103±2.8	0.41
Diastolic Blood Pressure, mmHg	64±2.6	71 ±2.2	0.03
Mean Right Atrial Pressure, mmHg	12±2.0	12±1.7	0.96
Systolic Pulmonary Artery Pressure, mmHg	55±3.0	56±4.1	0.86
Diastolic Pulmonary Artery Pressure, mmHg	28±2.4	27±2.7	0.67
Pulmonary Capillary Wedge Pressure, mmHg	25±2.2	23±2.4	0.54
Cardiac Index, l/min/m^2	2±0.2	2±0.1	0.56
Pulmonary Vascular Resistance, Wood units	4±0.8	4±0.6	0.85
B-type Natriuretic Peptide, pg/mL	2280±418	1499±210.1	0.07
Creatinine, mg/dL	1 ±0.2	1 ±0.1	0.79
Sodium, mmol/L	133±1.6	134±0.9	0.57
Hemoglobin, g/dL	12±0.5	12±0.5	0.85

LVAD: left ventricular assist device, HF: heart failure, LVEDD: left ventricular end-diastolic diameter, LVEF: left ventricular ejection fraction. Responders (n=12), Non-responders (n=21). Values reported as mean ± SEM, *p*-values determined by one-way ANOVA and Sidak's multiple comparison test.

KEY RESOURCES TABLE

Reagent or resource	Source	Identifier
Antibodies		
MPC1	Cell Signaling Technology	14462S
MPC2	Cell Signaling Technology	46141S
MCT4/SLC16A3	Abcam	ab74109
α-Tubulin (DM1A)	Cell Signaling Technology	3873S
PDH	Cell Signaling Technology	3205S
p-PDH	Cell Signaling Technology	31866S
ANP	Santa Cruz Biotech	SC-515701
BNP	Santa Cruz Biotech	SC-271185
Citrate Synthase	Cell Signaling Technology	14309S
Calreticulin	Cell Signaling Technology	2891S
Pax5	Cell Signaling Technology	12709S
Alexa Fluor 488 phalloidin	Life Technology	A12379
Anti-IgG Goat Polyclonal Antibody (DyLight® 800)	Rockland Immunochemical	RL611-145-002
IRDye 680RD Donkey anti-mouse	LI-COR	926-68072
IRDye 800CW Donkey anti-rabbit	LI-COR	926-32213
Biological Samples		
HF patient / human LV heart tissue	U.T.A.H. Cardiac Transplant Program	N/A
Non-failing human donor heart tissue	U.T.A.H. Cardiac Transplant Program	N/A
Chemicals, Peptides, and Recombinant Proteins		
Corning™ DMEM with L-Glutamine, 4.5g/L Glucose and Sodium Pyruvate	Fisher Scientific	Corning™10013CM
Fetal Bovine Serum	Sigma Aldrich	F0926
Pen Strep	ThermoFisher	15140
Trypsin-EDTA (0.25%)	ThermoFisher	25200
Retinoic acid	Sigma Aldrich	R2625
PBS pH 7.4	Invitrogen	10010049
Polyethylenimine (PEI)	Sigma Aldrich	765090
Polybrene transfection reagent	EMD Millipore	TR-1003-G
Phenylephrine	Sigma Aldrich	P1240000
Isoproterenol	Sigma Aldrich	I5627
(-)-Isoproterenol hydrochloride	Sigma Aldrich	I6504-1G
Angiotensin II	Sigma Aldrich	A9525
UK-5099	Sigma Aldrich	PZ0160-5MG
Dimethyl Sulphoxide (DMSO) TC grade	Sigma Aldrich	D2650-100ML
0.9 % NaCl TC grade	Sigma Aldrich	S8776-100ML
VB124	This manuscript	N/A

Reagent or resource	Source	Identifier
Nitrocellulose blotting membrane 0.45 μm	GE Healthcare Amersham	10600002
LC/MS grade water	Fisher Scientific	W6-1
LC/MS grade methanol	Fisher Scientific	A456-1
[U-$^{13}C_6$]-Glucose	Cambridge	CLM-1396
Gibco™ DMEM, no glucose	Thermo Scientific	11-966-025
Fetal Bovine Serum, dialyzed, One Shot™	Thermo Scientific	A3382001
Primocin	InvivoGen	Ant-pm-2
Natural Mouse Laminin	Thermo Scientific	23017-015
HEPES	Thermo Scientific	15630080
Chemically Defined Lipid Concentrate	Thermo Scientific	11905031
Insulin-Transferrin-Selenium	Thermo Scientific	41400045
2,3-Butanedione monoxime	Sigma Aldrich	B0753-25G
Bovine Serum Albumin	Fisher Scientific	BP9705100
16% Paraformaldehyde	Fisher Scientific	50-980-487
TRITON X-100	Sigma	T9284
ProLong™ Diamond Antifade Mountant with DAPI	ThermoFisher Scientific	P36962
Methylcellulose	MP Biomedicals	155495
Tween-20	Sigma Aldrich	P1379-4L
Collegenase type II	Worthington Biochemical	
Protease type XIV	Sigma Chemical	P5147
Isoflurane	Vet One	NDC 13985-046-60
SYBR Green Supermix	Bio-rad	1725275
Oligonucleotides		
Fw (5′-3′) Primer for MPC1 gene: GTGCGGAAAGCGGCGGACTA	This manuscript	N/A
Rv (5′-3′) Primer for MPC1 gene: GGCAGCAATGGGAAGACCCCA	This manuscript	N/A
Fw (5′-3′) Primer for MPC1 gene: CGCGTTGGTGCGGAAAGCG	This manuscript	N/A
Rv (5′-3′) Primer for MPC1 gene: GGCAAATGTCATCCGCCCACT GA	This manuscript	N/A
Fw (5′-3′) Primer for MPC2 gene: CCTCCAGCCCGAGGGACC1 1 1	This manuscript	N/A
Rv (5′-3′) Primer for MPC2 gene: CATCGCCGCCGAGGGATCG	This manuscript	N/A
Fw (5′-3′) Primer for MPC2 gene: GCCCCCGCTCACCCAGGTATC	This manuscript	N/A
Rv (5′-3′) Primer for MPC2 gene: GGGAGCGTGGCTGTGTTCTCG	This manuscript	N/A
Fw (5′-3′) Primer for RPL32 gene: AAGTTCATCCGGCACCAGTCAGAC	This manuscript	N/A
Rv (5′-3′) Primer for RPL32 gene: ATCAGCAGCACTTCCAGCTCCTTG	This manuscript	N/A
Recombinant DNA		
piSMART mCMV-GFP shMPC1	Dharmacon	V3SR11254-238198885
piSMART mCMV-GFP shMPC1	Dharmacon	V3SR11254-243750046
piSMART mCMV-GFP sh non-targeting	Dharmacon	VSC11651
pMX-3XHA-GFP-Omp25	Gift from Dr. David Sabatini (MIT)	(Chen et al., 2017)

Reagent or resource	Source	Identifier
pMX-3XMyc-GFP-Omp25	Gift from Dr. David Sabatini (MIT)	(Chen et al., 2017)
lentiCas9-Blast	Addgene	Plasmid #52962-LV
Human CRISPR knockout pooled library	Addgene	#73178-LV
Critical Commercial Assays		
Pierce BCA protein assay kit	Thermo Scientific	23225
miRNeasyMini Kit	Qiagen	217004
RNAase free DNAase kit	Qiagen	79254
RNeasy Mini Kit	Qiagen	74104
High Capacity cDNA Reverse Transcription Kit	ThermoFisher Scientific	4368814
QIAamp® DNA Blood Maxi kit	Qiagen	51192
KAPA Library Complete Quantification Kits	Roche	07960140001
TruSeq Stranded RNA kit with Ribo-Zero Gold	Illumina	RS-122-2301
NovaSeq XP chemistry workflow	Illumina	20021664
NovaSeq S1 reagent Kit	Illumina	20027465
D1000 ScreenTape	Agilent Technologies	5067-5582
D1000 Reagents	Agilent Technologies	5067-5583
Deposited Data		
MPC1^{CKO} and WT murine heart RNAseq data	Gene Expression Omnibus	GEO: GSE152055
Experimental models: Cell Lines		
H9c2	ATCC	ATCC® CRL-1446™
H9c2 MPC1 KD	This manuscript	N/A
H9c2 shCtrl	This manuscript	N/A
H9c2 MPC1 OE	This manuscript	N/A
H9c2 EV	This manuscript	N/A
H9c2 Mito-tag	This manuscript	N/A
BT20	ATCC	ATCC® HTB-19™
MDA-MB-231	ATCC	ATCC® HTB-26™
Experimental Models: Organisms/Strains		
Mouse: C57BL/6J	Jackson Laboratories	Cat# 000664
Mouse: *MPC1*^{CKO}	This manuscript	N/A
Software and Algorithms		
Prism 8	Graphpad Software	https://graphpad.com
LI-COR Image Studio	LI-COR Biosciences	https://licor.com
STAR version 2.7.0f	(Dobin et al., 2013)	https://github.com/alexdobin/STAR
clumpify v38.34	Open source software	https://sourceforge.net/projects/bbmap
cutadapt	(Martin, 2011)	https://github.com/marcelm/cutadapt

Reagent or resource	Source	Identifier
featureCounts version 1.6.3	(Liao et al., 2014)	https://bioconductor.org/packages/release/bioc/html/Rsubread.html
MultiQC	(Ewels et al., 2016)	https://github.com/ewels/MultiQC
DESeq2 version 1.24.0	(Love et al., 2014)	https://bioconductor.org/packages/release/bioc/html/DESeq2.html
Gprofiler	(Reimand et al., 2007)	https://biit.cs.ut.ee/gprofiler/gost
Benjamini-Hochberg	(Benjamini and Hochberg, 1995)	N/A
XPRESSplot v0.2.2	(Berg et al., 2020)	https://github.com/XPRESSyourself/XPRESSplot
pandas	The pandas development team	https://github.com/pandas-dev/pandas
NumPy	(Harris et al., 2020)	https://github.com/numpy/numpy
Scikit-Learn	(Pedregosa et al., 2011)	https://github.com/scikit-learn/scikit-learn
Matplotlib	(Hunter, 2007)	https://github.com/matplotlib/matplotlib
Seaborn	(M. Waskom and Seaborn contributors)	https://github.com/mwaskom/seaborn
Agilent Mass Hunter Qual B.07.00	Agilent	https://agilent.com
Agilent Mass Hunter Quant B.07.00	Agilent	https://agilent.com
MetaboAnalyst 4.0	(Xia and Wishart, 2011, Chong et al., 2018)	http://metaboanalyst.ca
Morpheus	Clustering web tool	https://software.broadinstitute.org/morpheus
ChemDraw 18.2	PerkinElmer Informatics	https://perkinelmer.com
Photoshop CC 2018	Adobe	https://adobe.com
Illustrator CC 2018	Adobe	https://adobe.com
BioRender	BioRender	https://biorender.com
Microsoft Excel	Microsoft	https://microsoft.com
ImageJ	NIH	https://imagej.nih.gov/iJ/
ZEN 2.3 pro	Carl Zeiss Microscopy	https://zeiss.com
Symyx Draw 3.1	MDL Information Systems	https://3dsbiovia.com
Vivo strain software (version 3.1.1)	Visual Sonics	N/A
R version 4.0.0	R Project	https://www.r-project.org
Other		
Waters GCT Premier Mass spectrometer	Waters	N/A
Agilent 6890 gas chromatograph	Agilent	N/A
Gerstal MPS2 autosampler	Gerstel	N/A

Reagent or resource	Source	Identifier
Zeiss Axio Observer Z1 microscope	Zeiss	https://zeiss.com
Olympus SZX10 microscope	Olympus	N/A
NovaSeq 6000	Illumina	N/A
CombiFlash Rf	Teledyne ISCO	https://teledyneisco.com
Mercury 400 MHz NMR spectrometer	Varian	https://varianinc.com
HP1050 HPLC system	Agilent	N/A
Vivo system	Catheter Precision Inc.	N/A
Leica SP8 confocal microscope	Leica	N/A
Osmotic minipumps	Alzet	No 2004-0.25ul/Hr 28days Pump
LightCycler 480 Real-Time PCR System	Roche	https://roche.com